2023

Large Eddy Simulation by using Wang's Liutex-based subgrid model

Vishwa Shah

Large Eddy Simulation

by using Wang's Liutex-based subgrid model

by

Vishwa Shah

Presented to the Faculty of the Graduate School of

The University of Texas at Arlington

in Partial Fulfillment of

the Requirements

for the Degree of

DOCTOR OF PHILOSOPHY

THE UNIVERSITY OF TEXAS AT ARLINGTON

August 2023

Acknowledgments

I am immensely grateful to my supervisor, Dr. Chaoqun Liu, who has been an exceptional mentor throughout my five-year Ph.D. program. His kindness, patience, and professionalism have been instrumental in guiding me towards conducting responsible research. Without his support, I wouldn't have been able to achieve my Ph.D. degree. Additionally, I would like to extend my appreciation to my colleagues Yonghua Yan, Yifei Yu, Oscar Alvarez, Charles Nottage, Yiqian Wang, and others who have played a role in my academic journey.

I want to express my gratitude to my committee members, Dr. Yue Liu (David), Dr. Guojun Liao, and Dr. Hristo Kojouharov, for their comprehension, encouragement, and expert academic guidance.

I want to express my gratitude to the Department of Mathematics for their financial assistance through the Graduate Teaching Assistantships program and the Benny M. McCarley Scholarship, as well as the College of Science for awarding me the Summer Dissertation Fellowship. This support has allowed me to concentrate on my research, and I appreciate it greatly.

I would like to express my sincere appreciation to my parents, Hasmukh Bhai Patel and Trushita Patel, and my husband, Deep Shah, as well as others who have offered their unwavering sacrifice, support, love, encouragement, and understanding.

August 4, 2023

Abstract

LARGE EDDY SIMULATION BY USING WANG'S LIUTEX-BASED SUBGRID MODEL

Vishwa D. Shah, Ph.D.

The University of Texas at Arlington, 2023

Supervising Professor: Chaoqun Liu

Turbulent flows and vortex structures in fluid dynamics have been captivating researchers for decades, owing to their intrinsic complexity and significance in various industrial and natural processes. Despite their fundamental importance, the definition and identification of vortices in turbulent flows continue to pose challenges, and to date, no universally accepted approach exists. This pursuit dates to the pioneering work of Hermann von Helmholtz in the 19th century, when the concept of vortices was first introduced.

In 2019, Liu et al. introduced a novel physical quantity termed "Liutex" in scalar, vector, and tensor forms, providing a promising avenue for understanding and characterizing turbulent flows. The Liutex approach offers a comprehensive framework for vortex identification, addressing issues that plagued previous methods and paving the way for more accurate simulations and analysis of turbulent flows. Building upon this foundation, our research seeks to explore the potential of Liutex in improving Large Eddy

Simulation (LES) techniques.

The primary objective of this study is to investigate the effectiveness of Wang's Liutex-based subgrid model for LES in capturing the intricate dynamics and structure of turbulent flows. The research methodology involves conducting extensive numerical simulations and data analysis using high-performance computing resources. The computational results are recorded and analyzed to study the mean velocity profile and flow characteristics.

Wang's Liutex-based subgrid model is implemented within the framework of LES, allowing for the representation of small-scale fluid motions such as eddies, swirls, and vortices. These subgrid-scale features are not fully resolved in LES, and subgrid models like Liutex are essential in bridging the gap between resolved and unresolved motions, improving the accuracy and predictive capabilities of the simulations. The new model will be tested in two LES coarse grid models, a LES that is 8 times more coarse than DNS and 32 times more coarse than DNS.

The research also explores the capability of Liutex to accurately identify and characterize vortices in turbulent flows. By quantitatively assessing vortex strength, rotational axes, vortex core locations, and sizes, the Liutex-based subgrid model offers insights into the underlying mechanisms of turbulent flows that were previously difficult to ascertain.

Additionally, the application of Liutex in LES enables the study of transitional flow regimes, where the transition from laminar to turbulent flow occurs. This aspect of the

research expands the understanding of flow stability and transition mechanisms, which have significant implications in engineering applications and natural phenomena.

In conclusion, this study highlights the potential of the Liutex-based subgrid model as a powerful tool for enhancing Large Eddy Simulation of turbulent flows. By leveraging Liutex, researchers and engineers can gain a deeper understanding of the complex dynamics and structures present in turbulent flows, leading to improved predictive models and design strategies in various industrial and environmental applications. The findings of this research contribute to the advancement of fluid dynamics research and pave the way for more accurate and efficient simulations of turbulent flows in the future.

Table of Contents

List of Illustrations

List of Tables

CHAPTER 1

INTRODUCTION

The presence of vortices is a ubiquitous phenomenon in nature, ranging from the violent swirling of tornadoes and hurricanes to the cosmic-scale rotations of galaxies. These swirling flows play a crucial role in the dynamics of many physical systems, including fluid turbulence. Most of the flows in nature and engineering applications are turbulent which means flow fluctuates rapidly in time and space. Examples of such flows are oceanic currents, flow over the wing of an aircraft, flow over the turbine blade. In everyday life, some of the flows are observed in the stirring of coffee, and water running through taps. Turbulent flows are characterized by the presence of countless vortices of varying sizes and strengths, and understanding their behavior is essential for advancing our understanding of many natural and engineering processes.

Osborne Reynolds produced the first known visualization of a flow changing from laminar to turbulent motion in 1883. In his experiment, Reynolds used ink as a dye to study the flow of water in a glass tube. The dye traveled down the tube in a continuous, straight line at lower flow rates. A fascinating occurrence, however, emerged when the flow rate rose: the colorful dye abruptly blended with the surrounding water, filling the remainder of the tube with a turbulent flow. Reynolds created a dimensionless number, now known as the Reynolds number (Re), to statistically assess these experimental results. $Re = U * L / v$ is the formula for the Reynolds number, where U stands for the velocity scale, L for the

length scale, and for the kinematic viscosity. Reynolds established a critical threshold over which the flow turns turbulent by looking at the Reynolds number in his classic article. This dimensionless quantity governs the dynamic similarity of viscous flows by describing the ratio of the inertial and viscous forces acting on a fluid particle. It has now become a key parameter in fluid mechanics. Unquestionably, one of the most significant dimensionless quantities in the study of fluid dynamics is the Reynolds number.

The effects of friction inside the fluid cause the fluid elements in a thin layer near the surface of a solid body to move more slowly than the other fluid elements outside of this layer, which are unaffected. Typically, the boundary layer is used to describe this thin layer. The concept of the Boundary layer was first proposed by Ludwig Prandtl in 1905. He further emphasized that the viscous effects were negligible everywhere except in a thin layer close to the solid boundary of the body where the no-slip condition had to be fulfilled.

The phenomena of turbulent flow vary widely, but the governing equations describing the flow of the fluids are always the same. The equations are Navier-Stokes equations, which were first formulated in the 19^{th} century after Claude-Louis Navier and George Gabriel Stokes. A set of five equations with five variables (three velocity components, pressure, and scalar concentration) is developed. These equations include the continuity equation (conservation of mass), which determines the evolution of the scalar field, and the scalar transport equation. Only a few extremely simple flow scenarios have analytical solutions because the N-S equations are non-linear, time-dependent partial differential equations. Therefore, one must use supercomputers to numerically determine the solutions to the N-S equations.

However, turbulence remains one of the most challenging and enigmatic phenomena in fluid dynamics. One of the main reasons for this is the difficulty of defining and characterizing turbulence itself. Unlike laminar flows, which are characterized by smooth, regular motion, turbulent flows are characterized by complex, chaotic, and often unpredictable behavior. Features such as instability, irregularity in motion, compressibility, and difficulty in measuring turbulence are some of the mysterious features that make it hard to define turbulence.

Despite these challenges, significant progress has been made in recent decades in understanding and modeling turbulent flows. Direct numerical simulation commonly known as DNS became an important tool for challenging turbulence research (Moin and Mahesh, 1998). The Direct Numerical Simulation (DNS) data has been extensively used to model and visualize vortex structures in boundary layer transition using various vortex identification methods. In DNS, the scalar transport and time-dependent numerical solution are provided in three-dimensional. These equations need to be solved very accurately without using any turbulence models and so DNS must be performed on a very fine grid to capture all the scales eddies in the turbulent flow.

For instance, various vortex identification methods such as Liutex magnitude iso-surface, objective Liutex [1], Liutex-Omega method [2-3], Liutex core line method [4-5] and $Q, \Delta, \lambda_2, \lambda_{c_i}$ and Ω have been introduced and utilized to model and visualize vortex structures in boundary layer transition using Direct Numerical Simulation (DNS) data. These methods provide researchers with quantitative tools to extract and analyze the complex vortical structures present in turbulent flows. In particular, the third-generation vortex identification method based on the Liutex vector has been introduced to

mathematically define and extract vortical structures from experimental and numerical data. The definition is purely kinematic based on the velocity gradient tensor. The newly defined Rortex/Liutex is a physical quantity closely related to the turbulence structure and strength [6]. As noted by Pope [7], turbulence is a fundamental and ubiquitous phenomenon that plays a vital role in the transport of momentum, energy, and mass in fluids. In addition, turbulence can cause significant fluctuations in fluid properties and lead to complex flow patterns and structures. Ping Lu, Manoj T., and Y. Yan say turbulence is not generated by "vortex breakdown" but rather by positive and negative spikes and consequent high shear layers.

In the past few decades, large eddy simulation (LES) has emerged as a widely used and validated method for simulating turbulent flows, including transitional flows. In LES, the large-scale eddies are resolved directly, while the small-scale eddies are modeled via a sub-grid scale (SGS) stress modeling. Various SGS models have been proposed to model the kinetic energy contained by the filtered turbulence. According to Germano et al. [8], SGS modeling is the most critical and challenging aspect of LES for transitional flows, as the kinetic energy grows gradually in the transition region and is zero in the laminar region.

Several popular SGS models have been proposed, such as the Smagorinsky model, which is widely used due to its simplicity and computational efficiency. However, it has been found to be unable to reproduce the transition process accurately, as the sub-grid scale eddy viscosity calculated by the model is too large in the laminar region. The Wall-Adapting local Eddy Viscosity (WALE) model [9], which is based on the square of the velocity gradient tensor, has the ability in theory to simulate laminar flow and the development of linearly unstable waves.

The Smagorinsky model [11] is one of the first models introduced and widely used. On the turbulent-viscosity hypothesis, it assumes a linear relation between eddy-viscosity and the magnitude of large-scale deformation tensor. According to Wang et al. [10], the Liutex model performs better than the Smagorinsky model in decaying homogeneous isotropic turbulence (DHIT) and outperforms the WALE model. The Liutex model is based on the Liutex vector, which is a measure of the rotation of the flow and is calculated from the velocity gradient tensor.

In conclusion, LES is a promising method for simulating turbulent flows, but accurate prediction of boundary layer transition requires the development of appropriate SGS models. The Smagorinsky model, WALE model, and Liutex-based models are some of the popular SGS models used in LES for transitional flows, and their performance has been extensively studied and compared in various flow configurations.

In this dissertation, the analyses of the development of the Liutex, vorticity, and shear at the boundary layer transitions are done in detail. The development builds a strong background in sub-grid stress modeling. The data obtained from the flat plate case is analyzed with the different coarse grids 960*64*121 and 960*32*61 which are 8 times and 32 times more coarse than DNS for the subgrid scale Smagorinsky model and Liutex-Based proposed by Dr. Wang. The log-linear plot of the mean velocity is also studied, and the results are compared with DNS. The details of the study are given in Chapter 3 for the turbulence and computational models. Whereas the computational results are in Chapter 7.

CHAPTER 2

CASE SETUP AND GOVERNING EQUATIONS

2.1 Governing Equations

The Navier-Stokes equations are the governing equations of fluid dynamics. In the 19th century, these equations were first derived by Claude-Louis Navier and George Gabriel Stokes.

The 3D compressible Navier-Stokes equations in the curvilinear coordinates can be written in the following conservative form:

$$\frac{1}{J}\frac{\partial \boldsymbol{Q}}{\partial t}+\frac{\partial(\boldsymbol{E}-\boldsymbol{E}_v)}{\partial \xi}+\frac{\partial(\boldsymbol{F}-\boldsymbol{F}_v)}{\partial \eta}+\frac{\partial(\boldsymbol{H}-\boldsymbol{H}_v)}{\partial \zeta}=0 \tag{2.1}$$

The vector of conserved quantities $\boldsymbol{Q}$, inviscid flux vector$(\boldsymbol{E},\boldsymbol{F},\boldsymbol{H})$, and viscous flux vector $(\boldsymbol{E_v},\boldsymbol{F_v},\boldsymbol{H_v})$ are defined as

$$\boldsymbol{Q}=\begin{pmatrix}\rho\\ \rho u\\ \rho v\\ \rho w\\ e\end{pmatrix}, \tag{2.2}$$

$$\boldsymbol{E}=\frac{1}{J}\begin{pmatrix}\rho U\\ \rho uU+p\xi_x\\ \rho vU+p\xi_y\\ \rho wU+p\xi_z\\ (e+p)U\end{pmatrix}, \tag{2.3}$$

$$\boldsymbol{F} = \frac{1}{J}\begin{pmatrix} \rho V \\ \rho u V + p\eta_x \\ \rho v V + p\eta_y \\ \rho w V + p\eta_z \\ (e+p)V \end{pmatrix}, \tag{2.4}$$

$$\boldsymbol{H} = \frac{1}{J}\begin{pmatrix} \rho W \\ \rho u W + p\zeta_x \\ \rho v W + p\zeta_y \\ \rho w W + p\zeta_z \\ (e+p)W \end{pmatrix} \tag{2.5}$$

$$\boldsymbol{E}_v = \frac{1}{J}\begin{pmatrix} 0 \\ \tau_{xx}\xi_x + \tau_{yx}\xi_y + \tau_{zx}\xi_z \\ \tau_{xy}\xi_x + \tau_{yy}\xi_y + \tau_{zy}\xi_z \\ \tau_{xz}\xi_x + \tau_{yz}\xi_y + \tau_{zz}\xi_z \\ q_x\xi_x + q_y\xi_y + q_z\xi_z \end{pmatrix} \tag{2.6}$$

$$\boldsymbol{F}_v = \frac{1}{J}\begin{pmatrix} 0 \\ \tau_{xx}\eta_x + \tau_{yx}\eta_y + \tau_{zx}\eta_z \\ \tau_{xy}\eta_x + \tau_{yy}\eta_y + \tau_{zy}\eta_z \\ \tau_{xz}\eta_x + \tau_{yz}\eta_y + \tau_{zz}\eta_z \\ q_x\eta_x + q_y\eta_y + q_z\eta_z \end{pmatrix} \tag{2.7}$$

$$\boldsymbol{E}_v = \frac{1}{J}\begin{pmatrix} 0 \\ \tau_{xx}\zeta_x + \tau_{yx}\zeta_y + \tau_{zx}\zeta_z \\ \tau_{xy}\zeta_x + \tau_{yy}\zeta_y + \tau_{zy}\zeta_z \\ \tau_{xz}\zeta_x + \tau_{yz}\zeta_y + \tau_{zz}\zeta_z \\ q_x\zeta_x + q_y\zeta_y + q_z\zeta_z \end{pmatrix} \tag{2.8}$$

where J is the Jacobian of the coordinate transformation between the curvilinear (ξ, η, ζ) and Cartesian frames(x, y, z), and $\xi_x,\ \xi_y,\ \xi_z,\ \eta_x,\ \eta_y,\ \eta_z,\ \zeta_x,\ \zeta_y,\ \zeta_z$ are coordinate transformation metrics. The contravariant velocity components (U, V, W) are defined as

$$U = u\xi_x + v\xi_y + w\xi_z,\ V = u\eta_x + v\eta_y + w\eta_z, W = u\zeta_x + v\zeta_y + w\zeta_z.$$

e is the total energy and defined as

$$e = \frac{p}{\gamma-1} + \frac{1}{2}(u^2 + v^2 + w^2) \tag{2.9}$$

The components of viscous stress and heat flux are denoted by $\tau_{xx},\ \tau_{yx},\ \tau_{zx}, \tau_{xy},\ \tau_{yy},\ \tau_{zy}, \tau_{xz},\ \tau_{yz},\ \tau_{zz}$ and $q_x,\ q_y,\ q_z$, respectively.

In the dimensionless form of Eq. (2.1), the reference values for length, density, velocities, temperature, and pressure are δ_{in}, ρ_∞, U_∞, T_∞ and $\rho_\infty U_\infty^2$, where δ_{in} is the displacement thickness of inflow. The resulting parameters, Mach number, and Reynolds number, are expressed as

$$M_\infty = \frac{U_\infty}{\sqrt{\gamma R T_\infty}}, \tag{2.10}$$

$$Re = \frac{\rho_\infty U_\infty \delta_{in}}{\mu_\infty}, \tag{2.11}$$

$$\mathrm{Pr} = \frac{\mathrm{C_p}\mu_\infty}{k_\infty}, \tag{2.12}$$

$$\gamma = \frac{C_p}{C_v} \tag{2.13}$$

where R is the ideal gas constant, γ the ratio of specific heat, C_p is the Specific Heat at Constant Pressure, C_v is the Specific Heat at Constant volume, and μ_∞ the viscosity.

2.2 Numerical Methods

A sixth-order compact scheme is used for the spatial discretization in the stream-wise and wall-normal directions. For internal points $i = 3, \dots, N-2$, the sixth-order compact scheme is as follows

$$\frac{1}{3}f'_{i-1} + f'_{i-1} + \frac{1}{3}f'_{i-1} = \frac{1}{h}\left(-\frac{1}{36}f_{i-2} - \frac{7}{9}f_{i-1} + \frac{7}{9}f_{i+1} + \frac{1}{36}f_{i+2}\right) \tag{2.14}$$

where f'_i is the derivative at point i. The fourth-order compact scheme is used at points $i = 2$ and $N-1$, and the third-order one-sided compact scheme is used at the boundary. In the spanwise direction where periodic conditions are applied, the pseudo-spectral method is used. To eliminate the spurious numerical oscillations caused by central difference schemes, instead of using artificial dissipation, an implicit sixth-order compact scheme for space filtering is applied to the primitive variables after a specified number of time steps. The governing equations are solved explicitly in time by a third-order TVD Runge–Kutta scheme:

$$\boldsymbol{Q}^{(0)} = \boldsymbol{Q}^{n} \tag{2.15}$$

$$\boldsymbol{Q}^{(1)} = \boldsymbol{Q}^{(0)} + \Delta t \boldsymbol{R}^{(0)} \tag{2.16}$$

$$\boldsymbol{Q}^{(2)} = \frac{3}{4}\boldsymbol{Q}^{(0)} + \frac{1}{4}\boldsymbol{Q}^{(1)} + \frac{2}{4}\Delta t \boldsymbol{R}^{(1)} \tag{2.17}$$

$$\boldsymbol{Q}^{(3)} = \frac{1}{3}\boldsymbol{Q}^{(0)} + \frac{2}{3}\boldsymbol{Q}^{(2)} + \frac{1}{3}\Delta t \boldsymbol{R}^{(2)} \tag{2.18}$$

$$\boldsymbol{Q}^{n+1} = \boldsymbol{Q}^{(3)} \tag{2.19}$$

The methods have been developed into a DNS code – "DNSUTA" [12,13,14], which has been validated by NASA Langley and UTA carefully to make sure that the DNS results are correct. The detailed code validation has been reported by Liu and Chen [15].

2.3 Simulation case and code validation

The Direct Numerical Simulation (DNS) technique is utilized to investigate the boundary layer flow transition on a flat plate. The physical domain and coordinate system are depicted in Figure 3. Here, x_{in}represents the distance between the leading edge of the plate and the inlet of the simulation domain, while $L_x$and L_y denote the lengths of the computational domain in the streamwise and spanwise directions, respectively. Additionally, L_{zin} represents the height of the inlet. Detailed specifications can be found in Table 1. The grid used has dimensions of 1920×128×241, corresponding to the number of grid points in the streamwise, spanwise, and wall-normal directions. Grid stretching is applied in the normal direction, while the streamwise and spanwise directions are kept uniform.

To ensure accurate representation, the length of the first grid layer in the normal direction at the entrance is set to 0.43 in wall units (z+ = 0.43). A Jacobian coordinate transformation is employed to map the physical domain to the computational domain, as illustrated in Figure 0. The inflow parameters, such as the Mach number and Reynolds number, are listed in Table 2. At the wall boundary on the flat plate, adiabatic and non-slipping conditions are imposed. Non-reflecting boundary conditions are applied at the far field and outflow boundaries to simulate the flow behavior effectively. The inflow is given in the form of

$$q = q_{lam} + A_{2d}q'_{2d} + A_{3d}q'_{3d} \tag{2.20}$$

where q represents u, v, w, p u, v, w, p, and T, while q_{lam} is the Blasius solution for a two-dimensional laminar flat plate boundary layer. q'_{2d} and q'_{3d} are the 2-D and 3-D Tollmien-Schlichting (T-S) waves which are added into inflow as enforced perturbations and the amplitudes of the 2D, and 3D T-S waves are A_{2d} and A_{3d}. q'_{2d} and q'_{3d} have the following form:

$$q'_{2d} = q_{2d}e^{i(\alpha_{2d}x-\omega t)} \tag{2.21}$$

$$q'_{3d} = q_{3d}e^{i(\alpha_{3d}x\pm\beta y-\omega t)} \tag{2.22}$$

The streamwise wavenumber, spanwise wavenumber, frequency, and amplitude are $\alpha_{2d} = 0.29919 - i5.09586 \times 10^{-3}$, $\beta = \pm 0.5712$, $\omega = 0.114027$, $A_{2d} = 0.03$, $A_{3d} = 0.01$. The time step is set as $\Delta t = \frac{T}{20000}$ where T is the period of the T-S wave.

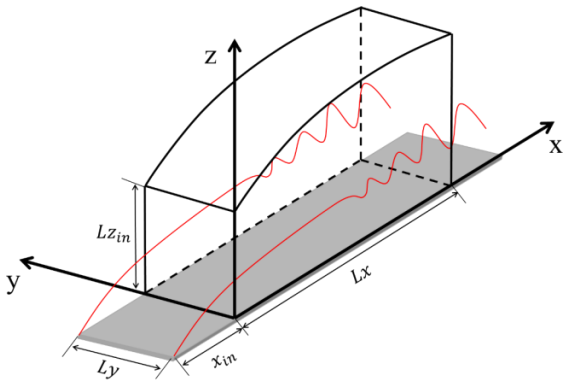

Figure2.1 Physical domain of simulation

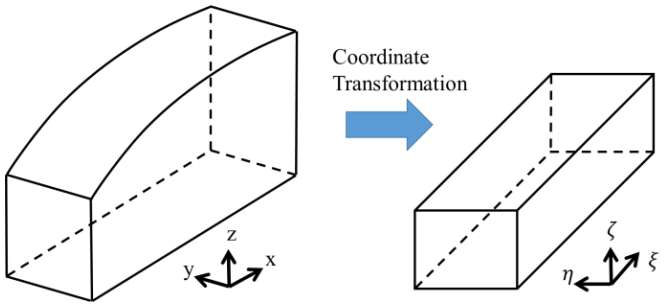

Figure 2.2 Coordinate transformation

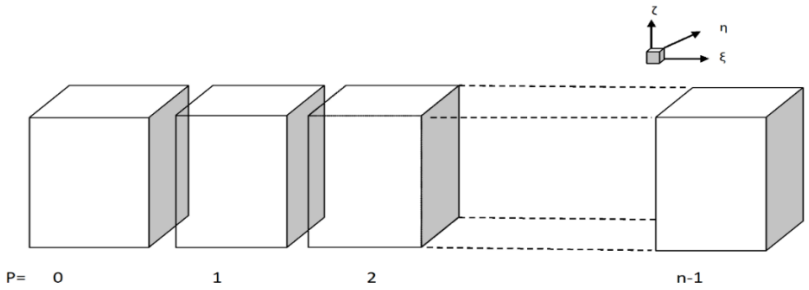

Figure 2.3 Computation domain

x_{in}	Lx	Ly	Lz_{in}	M_∞	Re	T_w	T_∞
$300.79\boldsymbol{\delta_{in}}$	$798.03\delta_{in}$	$22\delta_{in}$	$40\delta_{in}$	0.5	1000	273.15K	273.15K

Table 2.1 DNS parameters

The parameters in Table 2.1 are defined as follows:

x_{in} = distance between the leading edge of the flat plate and the upstream boundary of the computational domain

Lx = length of computational domain along x direction

Ly = length of the computational domain along y direction

Lz_{in} = height at the inflow boundary

M_{∞} = Mach number

Re = Reynolds number

T_w= wall temperature

T_{∞}= free stream temperature

The case and code validation has been introduced in the research [16], [17], [18].

The DNS code (DNSUTA) was validated by researchers from UTA and NASA Langley.

The results were compared to experiments and other's DNS results [19], [20] and the consistency shows that the code is correct and accurate.

CHAPTER 3

TURBULENCE MODELING AND COMPUTATIONAL METHODS

In fluid mechanics, based on the velocity levels or streamlines flow can be classified as laminar and turbulent flow. Turbulence in nature is a chaotic and unpredictable fluid motion that occurs when a fluid flows rapidly over a surface or through a confined space. Turbulent flow is characterized by high levels of velocity fluctuations and vortices, which mix and transport mass, momentum, and energy in a highly irregular manner. Turbulent flow consists of a coherent structure of eddies or vortices ranging from the smallest scale of motion to the largest scale of motion. The study involves the development of mathematical models and experimental techniques to describe and understand the complex behavior of fluid flows in turbulent regimes. Turbulence can be modeled using a variety of computational approaches, including direct numerical simulation (DNS), large eddy simulation (LES), and Reynolds-averaged Navier Stokes (RANS).

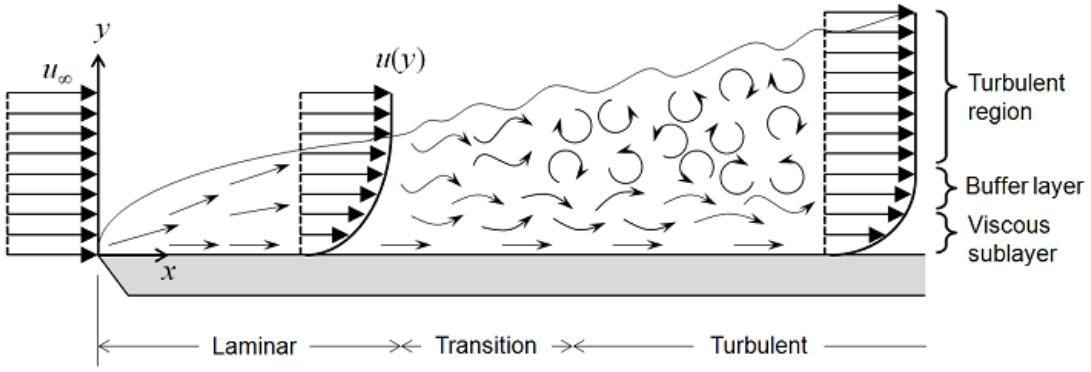

Figure 3.1 Turbulent flow and its sublayers.

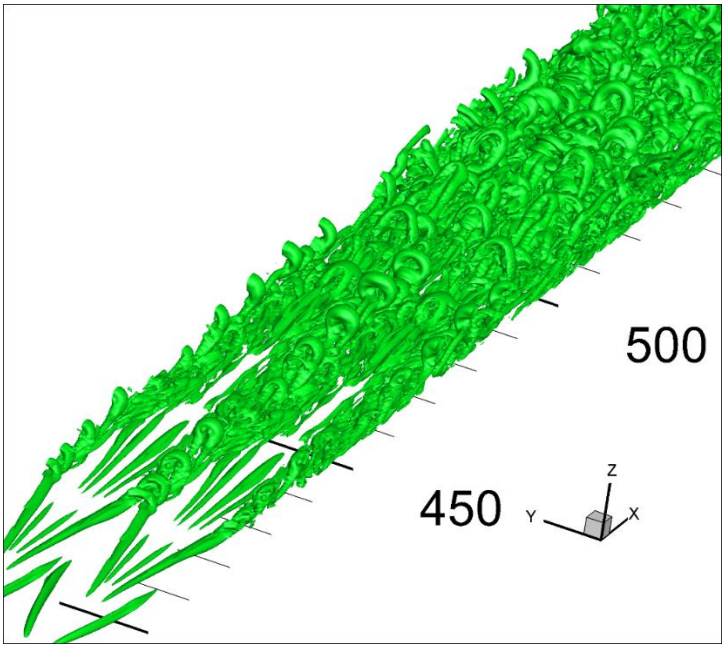

Figure 3.2 Vortex structures turbulent flat plate

3.1 Direct Numerical Simulation (DNS):

A DNS is a simulation in computational fluid dynamics in which the Navier-Stokes equations are numerically solved without any turbulence model. All the range of temporal and spatial scales must be resolved. Taking from the smallest dissipative scales (Kolmogorov scales), up to the integral scale L, containing most of the kinetic energy.

$$\text{The Kolmogorov scale, } \eta = \left(\frac{\nu^3}{\varepsilon}\right)^{\frac{1}{4}}$$

Where ν is the kinematic viscosity and ε is the rate of kinetic energy dissipation.

To satisfy the resolution requirements, the number N of points along a given mesh direction with increments h must be $Nh > L$, and $h \leq \eta$, so that the Kolmogorov scale can be resolved.

Since $\varepsilon \approx \frac{u'^3}{L}$, where u' is the root mean square of the velocity, which implies a 3-D DNS requires a number of mesh points N^3 satisfying $N^3 \geq Re^{\frac{9}{4}}$, where Re is the turbulent Reynolds number given as $Re = \frac{u'L}{v}$.

Therefore, the memory storage requirement in a DNS grows very fast with the Reynolds number. To get the accuracy, the integration must be done with a time step, Δt, small enough to move fluid particles only a fraction of the mesh spacing 'h' in each step. Which means,

$$C = \frac{u'\Delta t}{h} < 1 \text{ ; C is the Courant number.}$$

The total time interval simulated is proportional to the turbulence time scale τ given by

$$\tau = \frac{L}{u'}.$$

From all the above relations, and the fact that h must be the order of η, the number of time integration steps must be proportional to $L/(C\eta)$.

$$\frac{L}{\eta} \sim Re^{3/4}$$

We can estimate that the number of floating-point operations required to complete the simulation is proportional to the number of mesh points and the number of time steps which concludes that the number of operations grows as Re^3.

Thus, the computational cost of DNS is very high, even at low Reynolds numbers. It is a useful tool in fundamental research, however, the computational resources required by a DNS would exceed the capacity of the most powerful computers currently available.

3.2 Large Eddy Simulation (LES):

LES is the computational technique used in CFD to simulate turbulent flows. It was proposed by Joseph Smagorinsky in 1963. LES is applied in engineering applications such as simulation of the atmospheric boundary layer, acoustics, and flow configurations. LES is particularly useful for simulating complex turbulent flows where the wide range of scale from the large to small scales eddies. The traditional CFD cannot accurately model these flows and so it must rely on turbulence models to account for the small-scale eddies. As the DNS is computationally expensive, the LES is proposed to computationally reduce the cost by ignoring the smallest length scales, by low-pass filtering of the Navier-Stokes equations. The low pass filtering is the time and spatial averaging that removes small-scale information from the numerical solution.

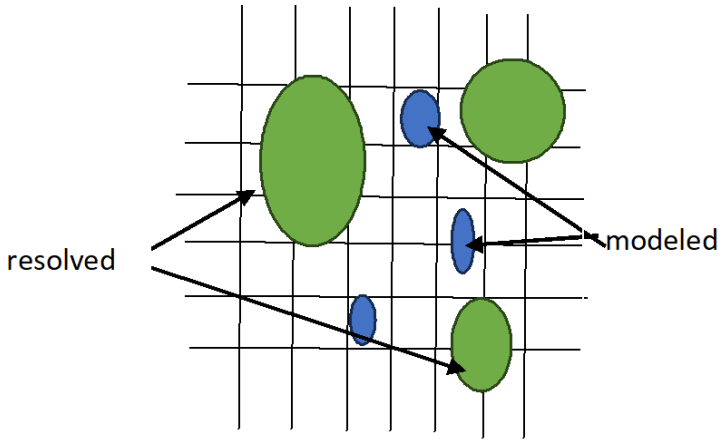

Figure 3.3 Large- and small-scale eddies

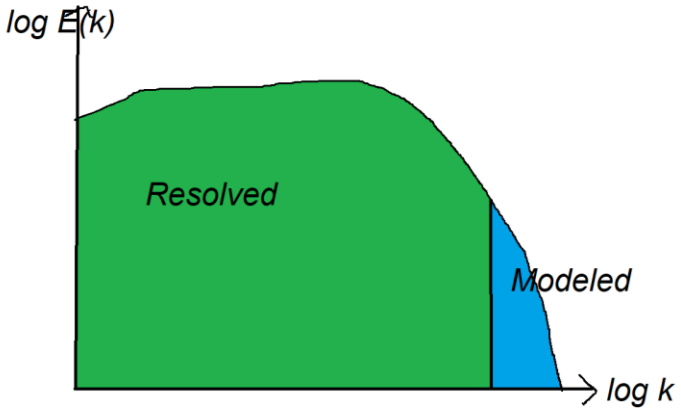

Figure 3.4 Energy Spectrum in LES

An LES filter can be applied to a spatial and temporal field and perform a spatial filtering operation, a temporal filtering operation, or both. The filtered field, denoted with a bar, is defined as:

$$\bar{u}_i(\vec{x}) = \int G(\vec{x} - \vec{\xi}) u(\vec{\xi})\, \mathrm{d}\vec{\xi} \tag{3.1}$$

Resulting in

$$u_\mathrm{i} = \bar{u}_i + u_\mathrm{i}' \tag{3.2}$$

Where $\bar{u}_i$ is the resolvable scale part and u_i' is the subgrid-scale part.

In most of the practical implementations, LES uses the grid as the filter to perform the explicit filtering. Some of the commonly used filters are the Box filter and the Gaussian filter.

The filtered equations are developed from the incompressible Navier-Stokes equations and the continuity equation. The filtered incompressible continuity equation,

$$\frac{\partial u_i}{\partial x_i} = 0 \tag{3.3}$$

The filtered Navier-Stokes equations,

$$\frac{\partial u_i}{\partial t} + u_j \frac{\partial u_i}{\partial x_j} = -\frac{1}{\rho}\frac{\partial p}{\partial x_i} + \frac{\partial}{\partial x_j}\left(v \frac{\partial u_i}{\partial x_j}\right) \tag{3.4}$$

Substituting in equation $u_\mathrm{i} = \bar{u}_i + u_\mathrm{i}'$ and $p = \bar{p} + p'$ and then filtering the resulting equation gives the equations of motion:

$$\overline{\frac{\partial u_i}{\partial t}} + \overline{\frac{\partial u_i u_j}{\partial x_j}} = -\overline{\frac{1}{\rho}\frac{\partial p}{\partial x_i}} + \overline{\frac{\partial}{\partial x_j}\left(v \frac{\partial u_i}{\partial x_j}\right)} \tag{3.5}$$

If filtering and differentiation commute, then

$$\frac{\partial \bar{u}_i}{\partial t} + \bar{u}_j \frac{\partial \bar{u}_i}{\partial x_j} = -\frac{1}{\rho}\frac{\partial \bar{p}}{\partial x_i} + \frac{\partial}{\partial x_j}\left(v \frac{\partial \bar{u}_i}{\partial x_j}\right) - \left(\overline{\frac{\partial u_i u_j}{\partial x_j}} - \frac{\partial \bar{u}_i \bar{u}_j}{\partial x_j}\right) \tag{3.6}$$

The extra term which arises from the non-linear advection terms because,

$$\overline{u_j \frac{\partial u_i}{\partial x_j}} \neq \bar{u}_j \frac{\partial \bar{u}_i}{\partial x_j} \tag{3.7}$$

Hence,

$$\tau_{ij} = \bar{u}_i \bar{u}_j - \overline{u_i u_j} \tag{3.8}$$

τ_{ij} is the residual stress tensor.

$$\frac{\partial \bar{u}_i}{\partial t} + \bar{u}_j \frac{\partial \bar{u}_i}{\partial x_j} = -\frac{1}{\rho}\frac{\partial \bar{p}}{\partial x_i} + \frac{\partial}{\partial x_j}\left(v\frac{\partial \bar{u}_i}{\partial x_j}\right) - \frac{\partial \tau_{ij}}{\partial x_j} \tag{3.9}$$

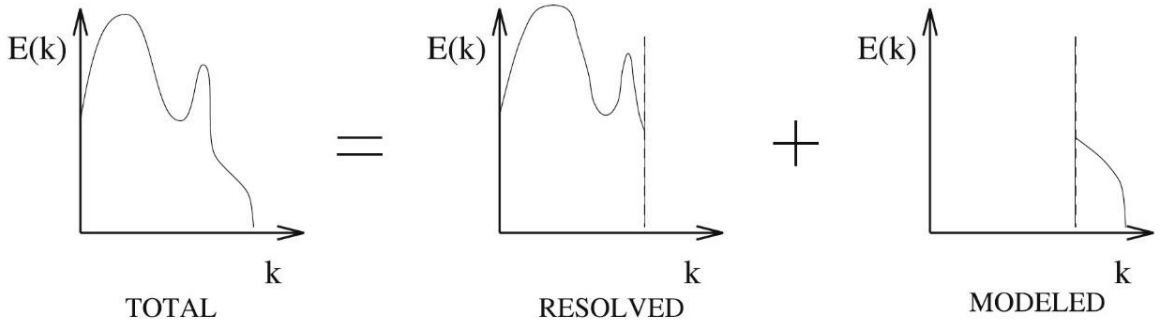

Figure 3.5 Decomposition of energy spectra of LES

In LES, there are two basic types of approach:

1. The implicit Large Eddy Simulation, in which no extra term is introduced in the governing equations, but the numerical method is chosen such that the numerical error and the resolution error will cancel each other.
2. The explicit Large Eddy Simulation, in which an extra forcing term, referred to as a sub-grid model is introduced in the governing equation to cancel the resolution error.

In the study, the explicit LES is used to best identify the sub-grid model with a less complicated formula and less computationally expensive.

3.3 Reynolds Average Navier-Stokes (RANS):

RANS is a time-averaged equation of motion for fluid flow. By performing the Reynolds decomposition, an instantaneous quantity is decomposed into its time-averaged and fluctuating quantities. The idea of this method was first proposed by Osborne Reynolds. To derive RANS equations the tool required from the Navier-Stokes equations is the Reynolds decomposition. Reynolds decomposition is nothing but the separation of the flow variable into the mean component and the fluctuating component. For an incompressible flow, the equations can be written as:

$$\frac{\partial u_i}{\partial x_i} = 0 \tag{3.10}$$

$$\frac{\partial u_i}{\partial t} + u_j \frac{\partial u_i}{\partial x_j} = f_i - \frac{1}{\rho}\frac{\partial p}{\partial x_i} + \frac{\partial}{\partial x_j}\left(v \frac{\partial u_i}{\partial x_j}\right) \tag{3.11}$$

Where f_i is a vector of external forces.

Now, each instantaneous quantity is split into time-averaged and fluctuating components, and the results are:

$$\frac{\partial \bar{u}_i}{\partial x_i} = 0 \tag{3.12}$$

$$\frac{\partial \bar{u}_i}{\partial t} + \bar{u}_j \frac{\partial \bar{u}_i}{\partial x_j} + \overline{u_\iota' \frac{\partial u_\iota'}{\partial x_j}} = \overline{f}_i - \frac{1}{\rho}\frac{\partial \bar{p}}{\partial x_i} + \frac{\partial}{\partial x_j}\left(v \frac{\partial \bar{u}_\iota}{\partial x_j}\right) \tag{3.13}$$

The momentum equation can also be written as,

$$\frac{\partial \bar{u}_i}{\partial t} + \bar{u}_j \frac{\partial \bar{u}_i}{\partial x_j} + \overline{u_\iota' \frac{\partial u_\iota'}{\partial x_j}} = \overline{f}_i - \frac{1}{\rho}\frac{\partial \bar{p}}{\partial x_i} + \frac{\partial}{\partial x_j}\left(v \frac{\partial \bar{u}_\iota}{\partial x_j}\right) - \frac{\overline{\partial u_\iota' u_j'}}{\partial x_j} \tag{3.14}$$

$$\rho \frac{\partial \bar{u}_i}{\partial t} + \rho\, \bar{u}_j \frac{\partial \bar{u}_i}{\partial x_j} = \rho \overline{f}_i + \frac{\partial}{\partial x_j}[-\bar{p}\, \delta_{ij} + 2\mu \overline{S}_{ij} - \overline{\rho u_i' u_j'}] \tag{3.15}$$

Where $\overline{S}_{ij} = \frac{1}{2}\left(\frac{\partial \bar{u}_i}{\partial x_j} + \frac{\partial \overline{u_j}}{\partial x_i}\right)$ is the rate of strain tensor.

$$\rho \overline{u_j} \frac{\partial \bar{u}_i}{\partial x_j} = \rho \overline{f_i} + \frac{\partial}{\partial x_j}\left[-\bar{P}\delta_{ij} + \mu\left(\frac{\partial \bar{u}_i}{\partial x_j} + \frac{\partial \overline{u_j}}{\partial x_i}\right) - \overline{\rho u_i' u_j'}\right] \tag{3.16}$$

The change in mean momentum of a fluid element caused by the mean flow's instability and convection by the mean flow is represented on the left side of this equation. The viscous stresses, the mean body force, the isotropic stress resulting from the mean pressure field, and the apparent stress($-\rho\overline{u'_i u'_j}$) resulting from the fluctuating velocity field, also known as the Reynolds stress, balance this change.

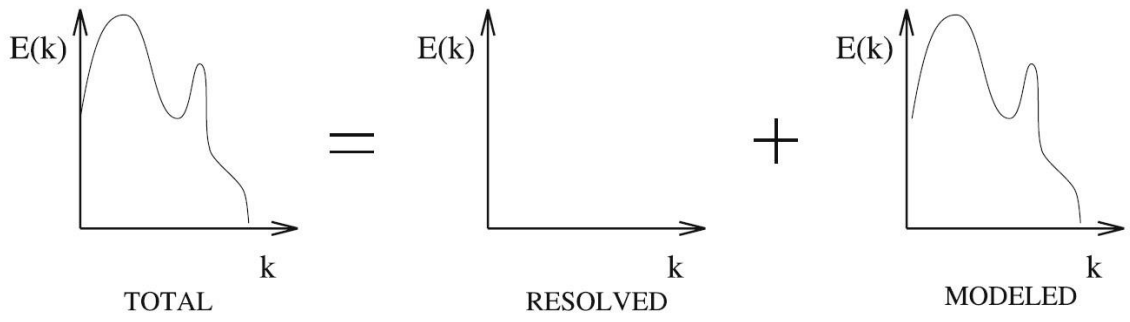

Figure 3.6 Decomposition of the energy spectra of RANS

3.4 Summary

LES is a powerful computational technique in CFD that has advantages over DNS and RANS methods for certain types of turbulent flow simulations. DNS resolves all scales of turbulence by providing accurate results. However, DNS is computationally expensive and requires massive computational resources. These can limit its applications to low Reynolds number flow or small-scale simulations. Whereas LES requires less computational cost and is suitable for high Reynolds number flows and larger simulations by providing accurate results. Whereas RANS solely rely on time-averaging equations that have a steady flow and cannot capture unsteady turbulent structures. LES models do not completely rely on fully empirical closure models like RANS, instead, they use dynamic subgrid-scale models that adapt the resolved flow structures. In regions of strong turbulence, LES is more reliable and less sensitive to assumptions. The eddies which are not resolved are modeled using different Subgrid scale models. In the present study, Wang's Liutex-based model is used to analyze the flat plate turbulent flow in the boundary layer.

CHAPTER 4

THREE GENERATION OF VORTEX IDENTIFICATION TECHNIQUES

Vortex structures are fundamental features of turbulent flows, playing a crucial role in the complexity and dynamics of such flows. To gain deeper insights into these intricate vortex structures, researchers have developed vortex identification methods aimed at visualizing and characterizing vortices in turbulent flows. This chapter introduces several prominent vortex identification methods that have been employed in this dissertation. The methods utilized in this research include the Omega method, Liutex, Liutex magnitude, Modified Omega-Liutex method, and Vortex core lines, which are considered part of the third generation of vortex identification methods based on the classification proposed by Liu et al. These third-generation methods have proven to be more robust and effective compared to earlier techniques.

Vortex identification methods can be categorized into three generations based on their underlying principles. The first-generation methods are based on vorticity, a measure of the local rotational motion of the fluid particles. However, these methods have limitations in capturing the full complexity of vortex structures in turbulent flows.

The second-generation methods encompass various criteria such as the $Q, \Delta, \lambda_2, \lambda_{c_i}$ parameters. These methods aim to define vortices based on specific flow properties but may still encounter challenges in accurately capturing the full range of vortex structures.

The third-generation methods, as introduced by Liu et al., represent a significant advancement in vortex identification. They were developed to address the limitations of the previous generations and have demonstrated superior performance in visualizing and characterizing vortices in turbulent flows. The Omega method, Liutex, Liutex magnitude, Modified Omega-Liutex method, and Vortex core lines are some of the key techniques belonging to this generation.

Throughout this chapter, a detailed explanation of each generation's methods will be provided, highlighting their strengths, weaknesses, and applicability to different flow scenarios. A comprehensive understanding of these vortex identification techniques will facilitate a deeper exploration of the complexities of turbulent flows and provide valuable insights for various engineering and scientific applications.

4.1 First Generation Methods

Earlier, from the Helmholtz vorticity tube proposal people used to believe that vortices consist of small vorticity tubes and the vortex strength is represented by the magnitude of the vorticity. The magnitude of the vorticity is nothing but the mathematical definition of velocity curl $\nabla \times v$.

$$\omega = \nabla \times \mathrm{v} = \begin{vmatrix} \mathrm{i} & \mathrm{j} & \mathrm{k} \\ \frac{\partial}{\partial \mathrm{X}} & \frac{\partial}{\partial \mathrm{Y}} & \frac{\partial}{\partial \mathrm{z}} \\ \mathrm{u} & \mathrm{v} & \omega \end{vmatrix} \tag{4.1}$$

Helmholtz originally defined vortex lines as lines drawn through a fluid mass, representing the direction of the momentary axis of rotation of water particles on the line. He also

introduced the concept of vortex filaments, which are portions of the fluid mass delineated by constructing corresponding vortex lines around an infinitely small surface element's circumference. These definitions led to three vortex theorems: (1) the constant strength of a vortex filament along its length, (2) the inability of a vortex filament to end within the fluid, requiring it to either extend to the fluid boundaries or form a closed path, and (3) the preservation of an initially irrotational fluid's irrotationality in the absence of external rotational forces.

Although the vorticity-based approach for detecting vortices is widely adopted and has been a guide for a long time, practical applications have revealed its limitations. Vorticity-based methods may not always accurately match the actual vortex structures. For instance, in a laminar boundary layer, the vorticity magnitude due to shear can be substantial, yet no rotational motion (vortex) is present. This discrepancy shows that a vortex cannot be exclusively described by vorticity, as the latter is unable to distinguish between regions of real rotation and shear layer regions.

In the near-wall regions of a laminar flow plane, the average shear force generated by the non-slip wall can be strong, resulting in a significant amount of vorticity but no observable rotation motions. Furthermore, the maximum vorticity magnitude does not necessarily correspond to the central region of vortex structures. Research by Wang et al. also indicates that the vorticity magnitude can be considerably reduced in the vortex core region near the solid wall in a flat plate boundary layer. Similarly, in turbulent boundary layers, the association between regions of strong vorticity and actual vortices can be weak, especially in the near-wall region.

These observations highlight the limitations of relying solely on vorticity-based methods for detecting vortices and emphasize the need for more sophisticated vortex identification techniques that can accurately capture the complex and dynamic nature of vortex structures in turbulent flows.

4.2 Second Generation Methods

The second-generation identification method is eigenvalue-based.

Suppose there are three eigenvalues of the velocity gradient tensor. Their characteristic equation can be as follows:

$$\lambda^3 + A\lambda^2 + B\lambda + C = 0, \tag{4.2}$$

Where,

$$A = -(\lambda_1 + \lambda_2 + \lambda_3) = -tr(\nabla v), \tag{4.3}$$

$$B = \lambda_1\lambda_2 + \lambda_2\lambda_3 + \lambda_3\lambda_1 = -\frac{1}{2}[tr(\nabla v^2) - tr(\nabla v)^2], \tag{4.4}$$

And $$C = -\lambda_1\lambda_2\lambda_3 = -\det(\nabla v) \tag{4.5}$$

A, B, and C are the three invariants of the velocity gradient tensor.

Q Criterion

The identification method is one of the best known and it was proposed by Hunt in 1988[21]. The method is expressed as follows:

$$Q = \frac{1}{2}(\|\boldsymbol{B}\|_F^2 - \|\boldsymbol{A}\|_F^2) \tag{4.6}$$

$$\text{Where } \mathbf{A}=\frac{1}{2}(\nabla v+\nabla v^{T})=\begin{bmatrix}\frac{\partial u}{\partial x} & \frac{1}{2}\left(\frac{\partial u}{\partial y}+\frac{\partial v}{\partial x}\right) & \frac{1}{2}\left(\frac{\partial u}{\partial z}+\frac{\partial w}{\partial x}\right)\\ \frac{1}{2}\left(\frac{\partial u}{\partial y}+\frac{\partial v}{\partial x}\right) & \frac{\partial v}{\partial y} & \frac{1}{2}\left(\frac{\partial v}{\partial z}+\frac{\partial w}{\partial y}\right)\\ \frac{1}{2}\left(\frac{\partial w}{\partial x}+\frac{\partial u}{\partial z}\right) & \frac{1}{2}\left(\frac{\partial w}{\partial y}+\frac{\partial v}{\partial z}\right) & \frac{\partial v}{\partial y}\end{bmatrix} \tag{4.7}$$

$$\text{And } \mathbf{B}=\frac{1}{2}(\nabla v-\nabla v^{T})=\begin{bmatrix}0 & \frac{1}{2}\left(\frac{\partial u}{\partial y}-\frac{\partial v}{\partial x}\right) & \frac{1}{2}\left(\frac{\partial u}{\partial z}-\frac{\partial w}{\partial x}\right)\\ \frac{1}{2}\left(\frac{\partial u}{\partial y}-\frac{\partial v}{\partial x}\right) & 0 & \frac{1}{2}\left(\frac{\partial v}{\partial z}-\frac{\partial w}{\partial y}\right)\\ \frac{1}{2}\left(\frac{\partial w}{\partial x}-\frac{\partial u}{\partial z}\right) & \frac{1}{2}\left(\frac{\partial w}{\partial y}-\frac{\partial v}{\partial z}\right) & 0\end{bmatrix} \tag{4.8}$$

Where **A** is the symmetric part and **B** is the anti-symmetric part of the velocity gradient tensor.

For Q>0 implies the existence of vortices, and the bigger Q is, the stronger the vortex is.

$\boldsymbol{\lambda_2}$ *criterion*

The λ_2 method was proposed by Jeong and Hussain in [22] 1995. The criteria are based on the observation that a local minimum pressure in a plane fails to identify vortices under strong unsteady and viscous effects. If the unsteady and viscous effects are neglected, then the symmetric part of the Navier-Stokes equations can be expressed as

$$A^2+B^2=-\nabla(\nabla p)/\rho, \tag{4.9}$$

where p is the pressure.

Moreover, Jeong and Hussain [22] define the vortex core as one connected region which has two negative eigenvalues of the symmetric tensor. If the eigenvalues are ordered in such a way that $\lambda_1 \geq \lambda_2 \geq \lambda_3$, then it is equivalent to saying that $\lambda_2 < 0$.

Even though these are two popular methods there are few limitations to using these methods.

1. $Q\ and\ \lambda_2$ are not able to capture the weak and strong vortices at the same time which makes it difficult to get the accurate vortex structures.
2. The physical meaning of Q and λ_2 is not clear.
3. A proper threshold is required for each case to identify appropriate vortex structures.

4.3 Third Generation Methods

Liutex an eigenvector-based vortex definition:

In 2017/2018, the Liutex vector was originally born. The vorticity decomposition to a rotational and non-rotational part. The idea behind the non-rotational part given by Liu is to extract the rigid rotation part from the fluid motion. Whereas the rotational part is defined as a Liutex vector, which can clearly represent both the direction and magnitude of the rotational motion. The mathematical definition of Liutex can be found as follows:

Definition: A local rotational axis is defined as the direction of **r**

where,

$$d\boldsymbol{v} = \alpha d\boldsymbol{r} \tag{4.10}$$

The definition means that there is no cross-velocity increment perpendicular to the direction of the local rotational axis. For example, if the z-axis is the rotational axis in a reference frame, the velocity can only increase or decrease along the z-axis, which means only $dw \neq 0$, but $du = 0$ and $dv = 0$. Liu et al [25], Gao and Liu [6] define that the

rotational strength is twice the minimal absolute value of the off-diagonal component of the 2×2 upper left submatrix and is given by

$$R = 2(\beta - \alpha), \beta^2 > \alpha^2 \tag{4.11}$$

$$R = 0, \alpha^2 \geq \beta^2 \tag{4.12}$$

The Liutex vector is obtained by,

$$\boldsymbol{R} = R\boldsymbol{r} \tag{4.13}$$

More details can be found in refs [6,26]. Wang et al. [27] recently derived an explicit formula to calculate the magnitude of $\boldsymbol{R}$, further simplifying the equation, the magnitude of R is obtained as

$$R = \langle \boldsymbol{\omega}, \boldsymbol{r} \rangle - \sqrt{\langle \boldsymbol{\omega}, \boldsymbol{r} \rangle^2 - 4\lambda_{ci}^2} \tag{4.14}$$

The Liutex vector can be defined as:

$$\boldsymbol{R} = R\boldsymbol{r} = \{ \langle \boldsymbol{\omega}, \boldsymbol{r} \rangle - \sqrt{\langle \boldsymbol{\omega}, \boldsymbol{r} \rangle^2 - 4\lambda_{ci}^2} \ \} \boldsymbol{r} \tag{4.15}$$

Where $\boldsymbol{\omega}$ is the vorticity vector.

The important thing here is to note that Liutex is a vector which provides both the local rotation axis and the rigid-body angular speed. Therefore, Liutex vectors, lines, and tubes can all be applied to describe vortex structures while all other vortex identification methods introduced above can only be used to show the iso-surface as a representation of the vortex boundaries, which is questionable. Moreover, the thresholds of these iso-surfaces are kind of arbitrary selection which are very different from case to case and the results are contaminated by shear because the only correct quantity to represent the rotational strength is the magnitude of Liutex.

The second third-generation method is the Omega-Liutex method. The method was developed by Liu and Liu [28] to overcome the issues of Q and λ_2 criterions. A small positive parameter ϵ is introduced to remove non-physical noises.

$$\Omega_R = \frac{\beta^2}{\alpha^2+\beta^2+\epsilon}, \tag{4.16}$$

$$\epsilon = b \times (\beta^2 - \alpha^2)_{max} \tag{4.17}$$

Where b is a small positive number.

The new Ω_R method can measure the relative rotation strength on the plane perpendicular to the local rotational axis. It can separate the rotational vortices from shear layers and non-physical structures. In comparison to other vortex identification methods, Ω_R does not require case-dependent thresholds and can always be set to 0.52 to get the vortex structures at different time steps in different cases.

CHAPTER 5

CORRELATION ANALYSIS BETWEEN SHOCK BOUNDARY LAYER INTERACTION AND LIUTEX

5.1 Introduction

SBLI is a subject that has gotten a lot of attention in recent decades (Dollin [29]). Shock wave boundary-layer interaction (SBLI) degrades flow quality by inducing large-scale flow separation, which can have a significant impact on aircraft and engine performance and frequently results in undesirable outcomes such as total pressure loss, flow instability, and distortion, engine unstart, drag rise, and high wall heating. In modern fluid dynamics, the study of SBLI is still a mystery. The process of SBLI involves both the incoming turbulent boundary layer and the subsequent separation zone. The extremely complicated flow brings extremely high difficulties in analyzing this problem. SBLI research has always focused on low-frequency noise. However, no consensus exists on the mechanism that causes low-frequency unsteadiness to occur. SBLI has a plethora of review papers (Delery and Marvin [30]; Dolling [31]; Smits and Dussauge [32]; Zheltovodov [35]; Andreopoulos et al. [33]; Lee [34]; Clement et al. [36]).

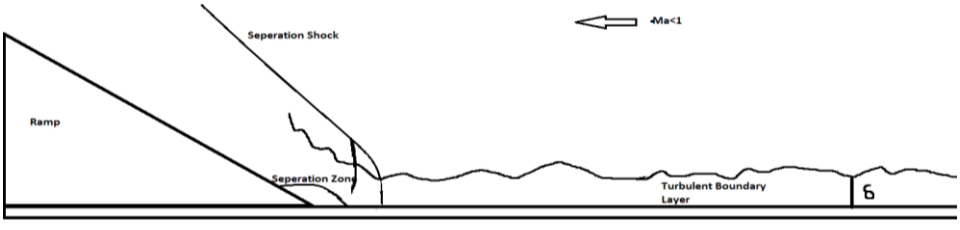

Figure 5.1 SBLI in a compressed corner

The instability of SBLI which researchers have studied for decades remains a mystery in modern fluid dynamics. Since the SBLI process involves both the incoming turbulent boundary layer and the subsequent separation zone, the flow is extremely complex, which brings extremely high difficulty to the analysis of this problem. Low-frequency noise has always been a key topic in SBLI's research. However, there is no widely accepted conclusion about the mechanism of low-frequency instability.

There are two primary schools of thought on the driving factor of low-frequency unsteadiness: upstream incoming flow variations or downstream instability. At Ma 5, Erengil and Dolling [37,38] conducted high-speed ramp flow studies. They discovered a strong link between shock-foot velocity and upstream boundary layer pressure changes. Unalmis and Dolling [39] proposed a mechanism for thickening and thinning. The superstructures can have a coherence of up to 40, according to Ganapathisubramani et al. [40]. At Ma 2.1, Humbel et al. [41] conducted trials with an incident SBLI. A series of studies on the statistical analysis between the low-frequency shock motion and the upstream/downstream flow fluctuation was proposed by Priebe and Martin [43]. However, an inherent instability in the downstream flow separation impacts the velocity and vorticity profiles in the initial stage of the SBLI. According to Clemens and Narayanaswamy [36], both upstream and downstream effects are always present in all shock-induced turbulent separated flows but the upstream mechanism dominates for strongly separated flows, and a combined mechanism dominates for weakly separated flows. Adding to it, Dupont et al. [42] computed the coherence between wall pressure changes around the reflected shock and places in the reattachment region was more than 0.8. According to Dong’s [44] latest study, the shock produced by a compression ramp flow at Ma = 2.5 is confirmed to have a

dominant low non-dimensional frequency. The interaction between the turbulent boundary layer and the separation shock wave/ ramp shock wave is investigated. The study involves the LES, to conduct the study of the supersonic ramp flow. To study the mechanics of low-frequency noises, power spectra of pressure, and occurrence of the passing vortices where the ramp shock wave is located are obtained and analyzed.

5.2 Case setup

In the study, a subzone in the middle of the whole domain of DNS simulation is selected which is halved in the spanwise direction. The main reason for choosing this subzone is that the flow is well developed of complex structures and relatively much data for different time steps. The power spectra of pressure and Liutex are obtained at $22 \times 22 \times 68 = 32{,}912$ points evenly distributed in the selected subzone. The x-coordinate varies from 624 to 944, the y-coordinate varies from 0.52 to 10.83, and the z varies from 0.6 to 13.8. Figure 5.2 gives the location of the subzone where the power spectra of pressure and Liutex were analyzed.

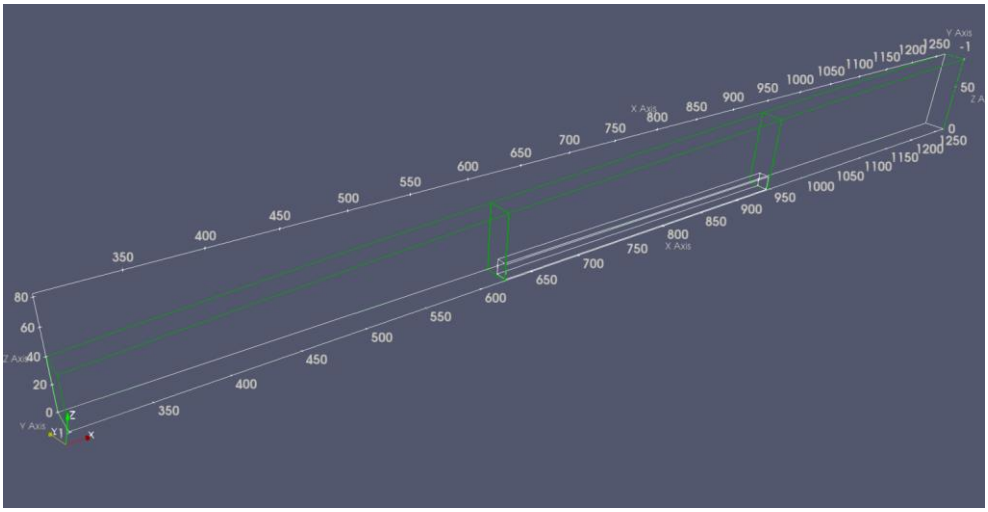

Figure 5.2 Domain of analysis

5.3 Results and Discussion

Complex vortex structures, such as lambda-vortices, hairpin vortices, and ring-like vortices, are a prominent characteristic of the transitional flow. In the previous work of the transition flow, the large-scale vortices are generated in the upper boundary layer by the multiscale shear layer in the flow [36,37]. The structures are quite robust and will gradually travel downstream and interact with the strong ramp shock. As shown in Figure 5.3, the ring-like vortices are visible from x=420δ_{d0} and the series of vortices are observed from x=500δ_{d0}. These structures are staggered in the streamwise direction. From x>600δ_{d0}, the structures of the ring-like vortices are broken, which leads to the generation of small-scale structures.

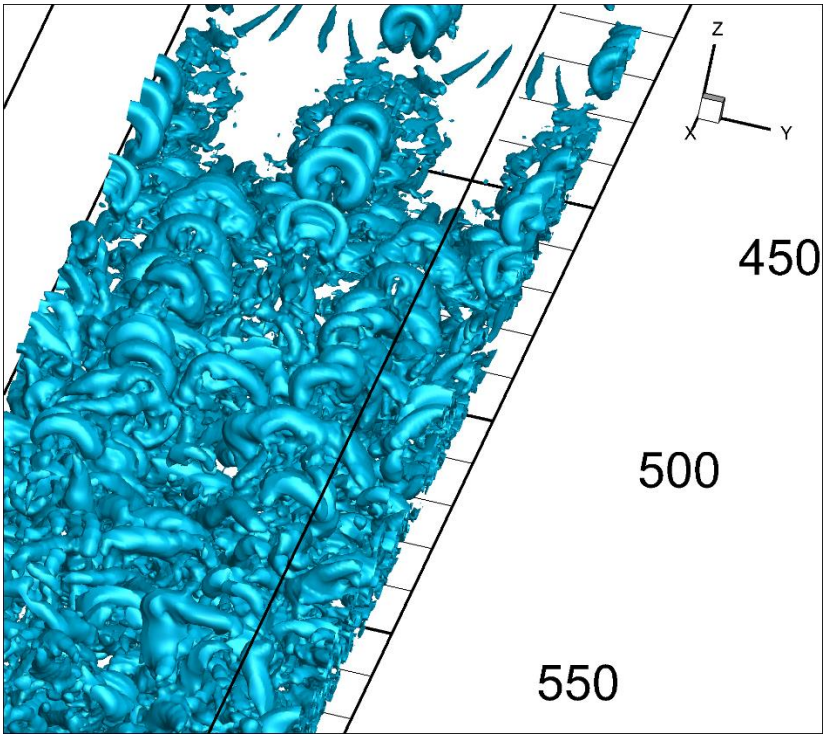

Figure 5.3 Ring-like vortex structures

Figure 5.4 (a-d) gives the distribution of correlation coefficients of pressure and Liutex spectra on YZ cross-sections (spanwise and normal directions). The white curve in each figure shows the locations of boundary layer thickness ($u/U_\infty = 99\%$), *the blue curves corresponds to the locations with* $y^+(z^+) = 30$ *and* 100. It can be clearly observed that below the boundary layer thickness, where exits variously scaled vortex structures, there it shows an extremely high correlation (colored in red).

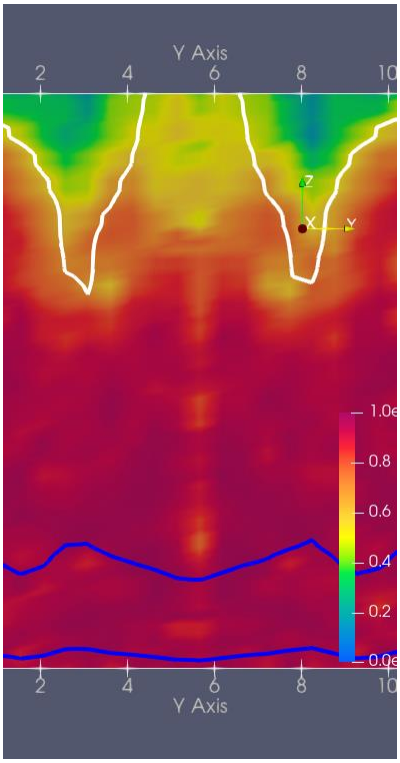

Figure 5.4 (c)

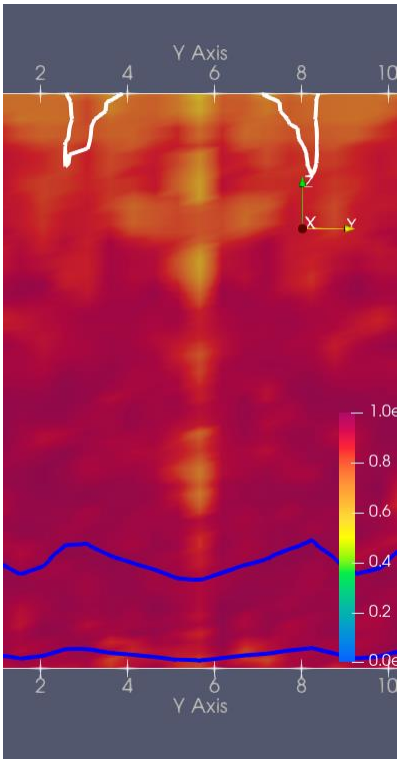

Figure 5.4 (d)

Figure 5.4 The distribution of correlation coefficients of pressure and Liutex

The correlation coefficient of pressure and Liutex spectra on XZ cross sections (streamwise and normal directions) is shown in Figure 5.5(a-d). The white curve in each figure shows the locations of boundary layer thickness (u/U_∞ = 99%), the blue curves correspond to the locations with $y^+(z^+) = 30\ and\ 100$. The extremely high correlation is observed below the boundary layer thickness, where variously scaled vortex structures exist.

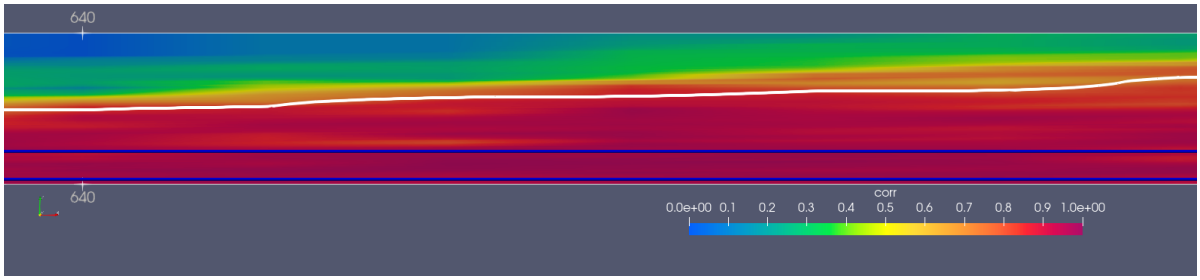

Figure 5.5 (a)

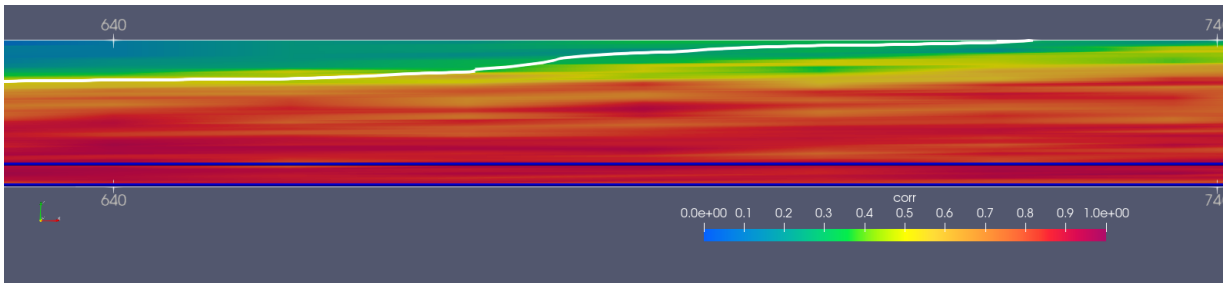

Figure 5.5 (b)

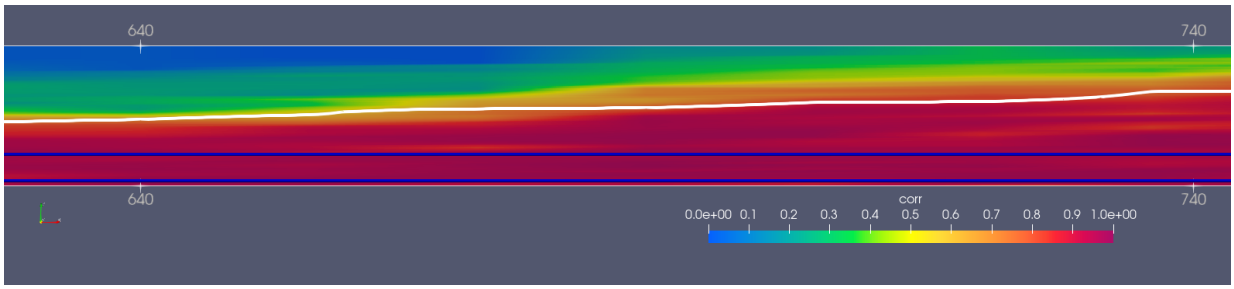

Figure 5.5 (c)

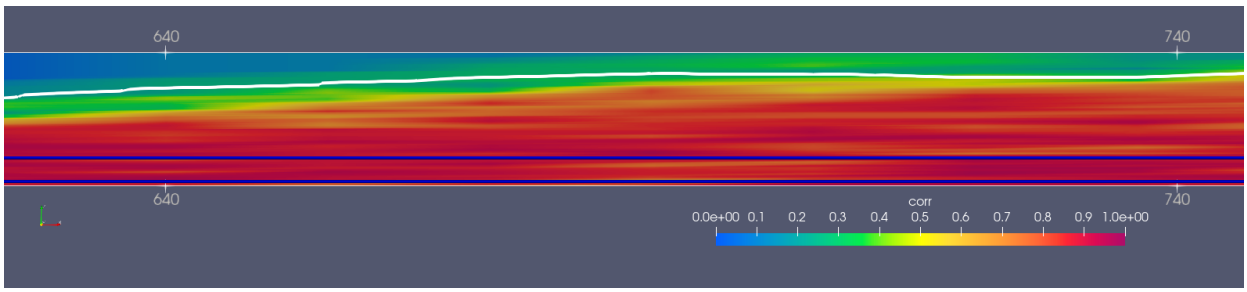

Figure 5.5 (d)

Figure 5.5 The correlation coefficient of pressure and Liutex spectra on the XZ cross-section

The distribution of correlation coefficients of pressure and Liutex spectra on XY cross sections (streamwise and spanwise directions) is given in Figure 5.6. It can be clearly observed that as we go closer to the bottom surface (above the viscous sublayer), the greater the correlation. Also, as the flow develops the correlation gradually increases.

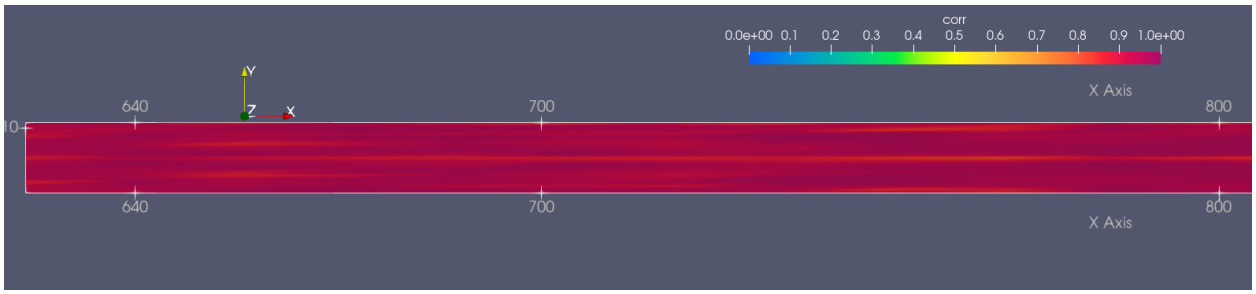

Figure 5.6 (a)

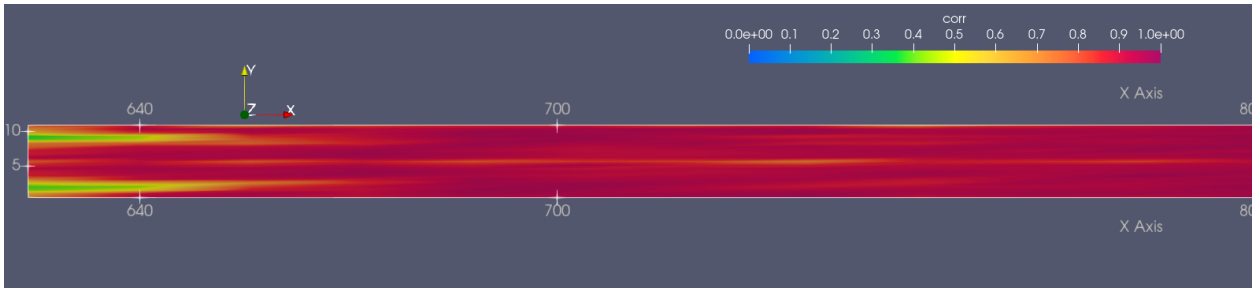

Figure 5.6 (b)

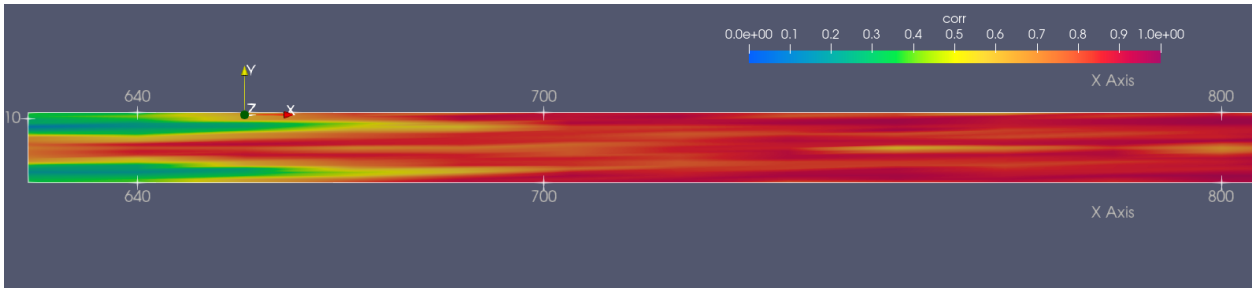

Figure 5.6 (c)

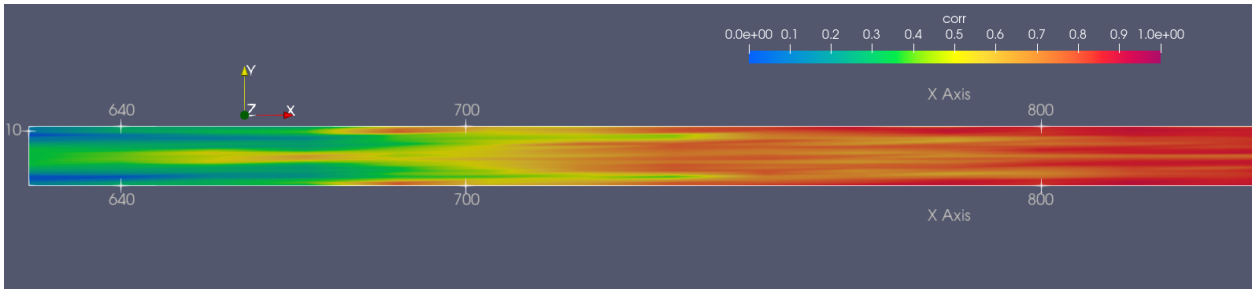

Figure 5.6 (d)

Figure 5.5 The correlation coefficient of pressure and Liutex spectra on the XY cross-section

Definition. The correlation coefficient is determined by dividing the covariance by the product of the two variables' standard deviations. Let x and y be the random variables with the sample size n, r(x,y) is the correlation coefficient of x and y if:

$$r(x,y) = \frac{cov(x,y)}{\sigma(x)\sigma(y)} \tag{5.1}$$

Where,

$$cov(x,y) = E\big[\big(x - E(x)\big)\big(y - E(y)\big)\big], \tag{5.2}$$

$$E(x) = \frac{1}{n}\sum_{i=1}^{n} x_i\,;\ x_i \text{ is the i}^{\text{th}} \text{ entry of x}, \tag{5.3}$$

$$Var(x) = E[\big(x - E(x)\big)^2], \tag{5.4}$$

$$\sigma(x) = \sqrt{Var(x)} \tag{5.5}$$

The Correlation Coefficient is a statistical concept revealing the extent to which two groups of data are related. If these two groups of data are entirely correlated their correlation is 1 and if they are irrelevant then their correlation coefficient is near zero.

Table 5.1 gives the corresponding correlations. By the qualitative analysis, the correlation coefficient is above 85%. Overall, a strong correlation between pressure and

Liutex is observed at every point. At the first 2 points, the correlation is relatively low because the points are in the upper boundary layer where the pressure fluctuation is less. On the other side, points 3-6 and 8-10 have a correlation of 90% due to the fact that they are located in the lower part of the boundary layer. Thus, by the power spectrum analysis of the vortex ring motion and Liutex, the results clearly show that the pressure fluctuation is closely related to the Liutex. The power spectra at 10 points of Liutex and pressure fluctuation are shown in Figure 5.7.

Points	**R**
1	**0.88**
2	**0.86**
3	**0.96**
4	**0.95**
5	**0.94**
6	**0.92**
7	**0.89**
8	**0.90**
9	**0.94**
10	**0.90**

Table 5.1 Correlation of 10 points

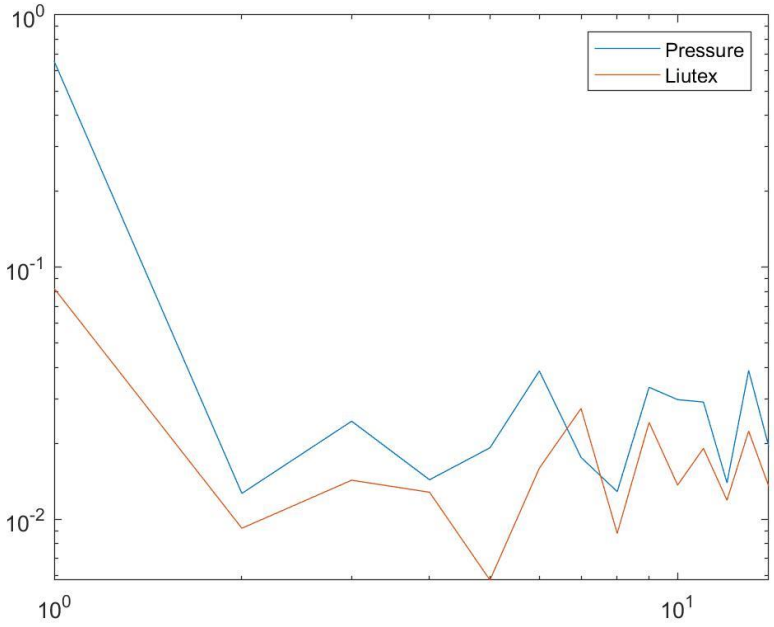

Figure 5.7(a) Power Spectra of Point 1

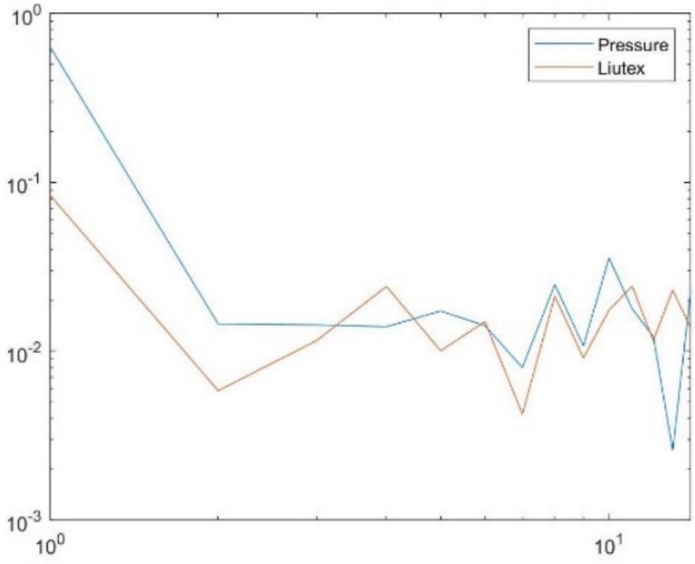

Figure 5.7 (b) Power spectra of Point 2

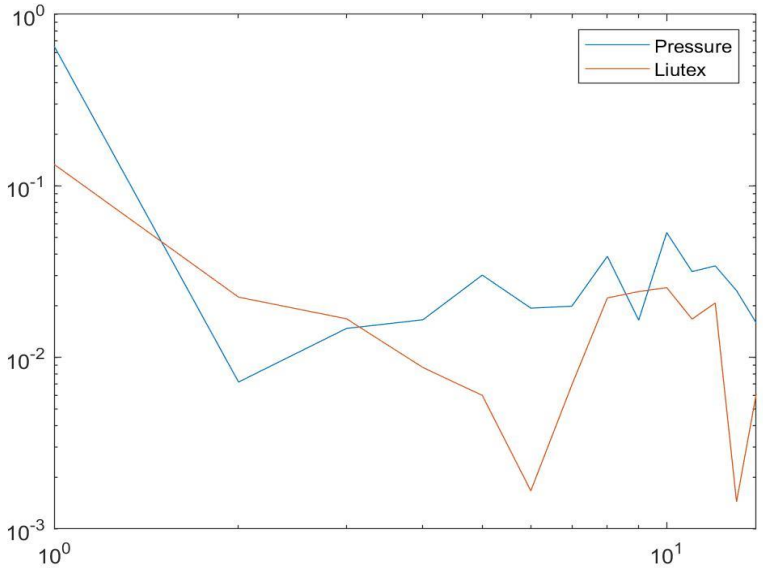

Figure 5.7 (c) Power Spectra of Point 3

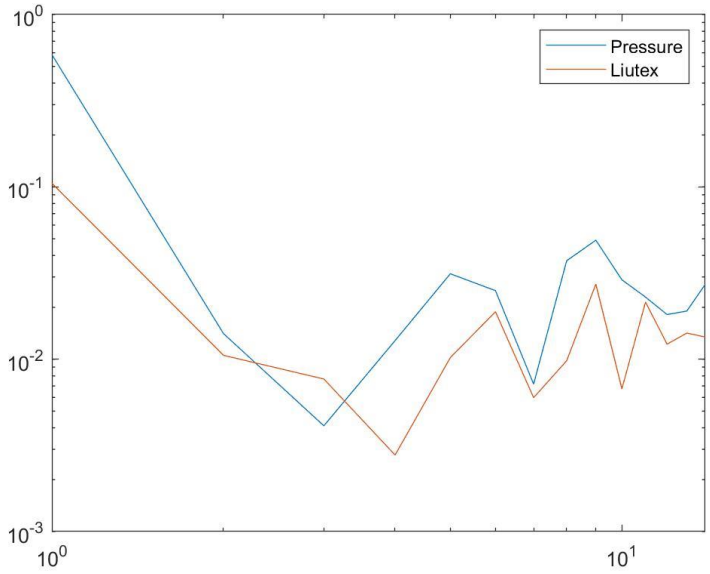

Figure 5.7 (d) Power Spectra of Point 4

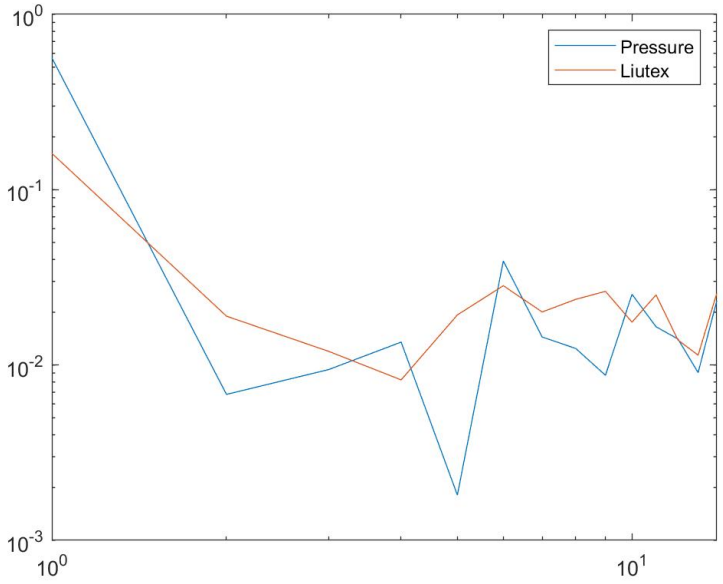

Figure 5.7 (e) Power Spectra of Point 5

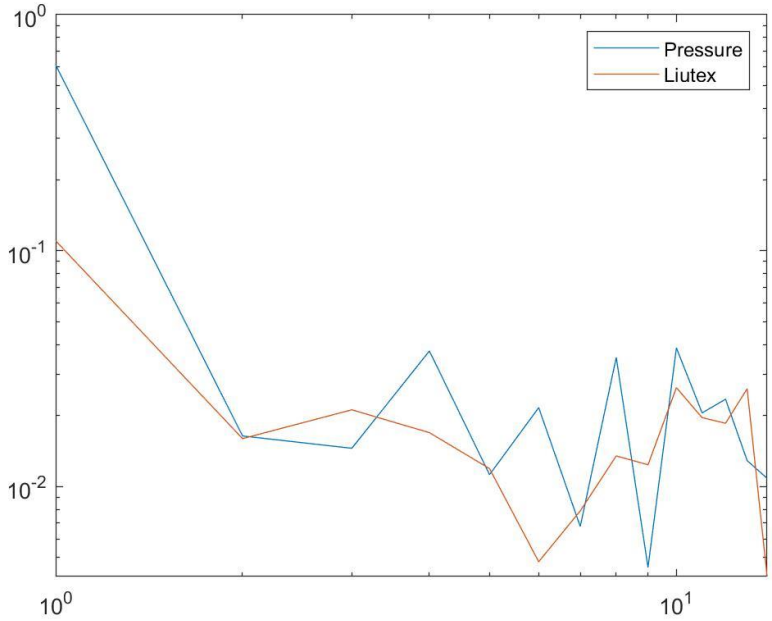

Figure 5.7 (f) Power Spectra of Point 6

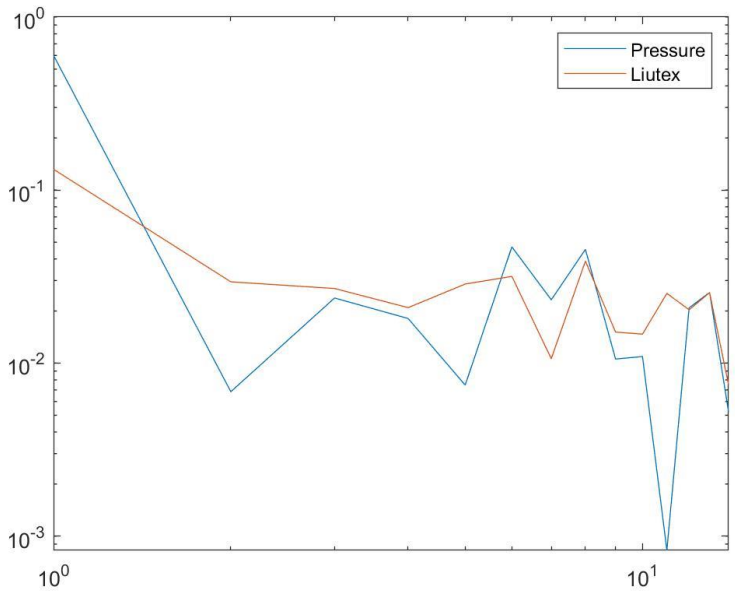

Figure 5.77 (g) Power Spectra of Point 7

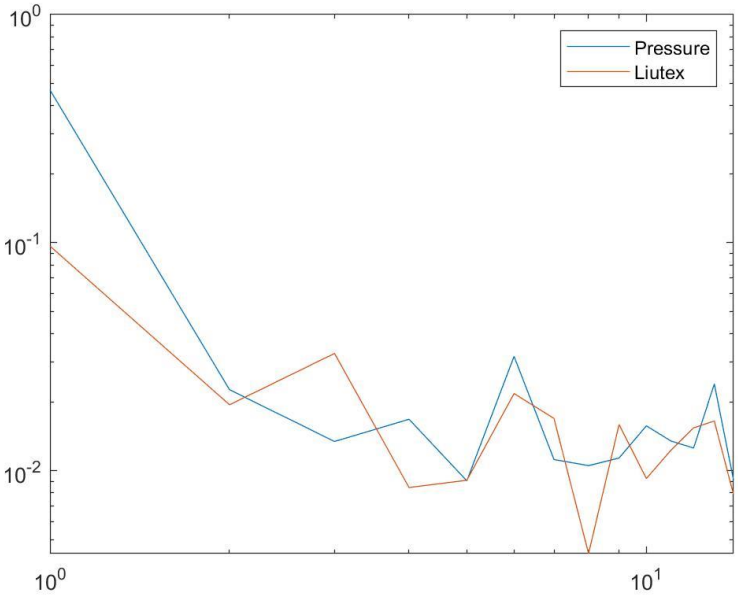

Figure 5.7 7 (h) Power Spectra of Point 8

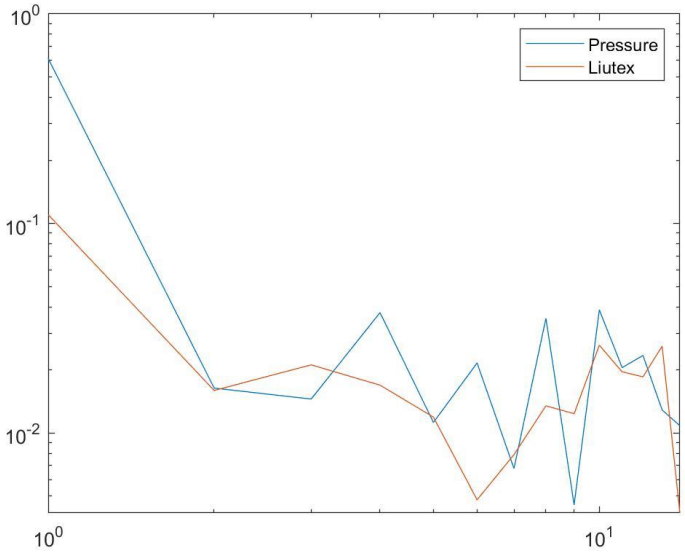

Figure 5.7 7 (i) Power Spectra of Point 9

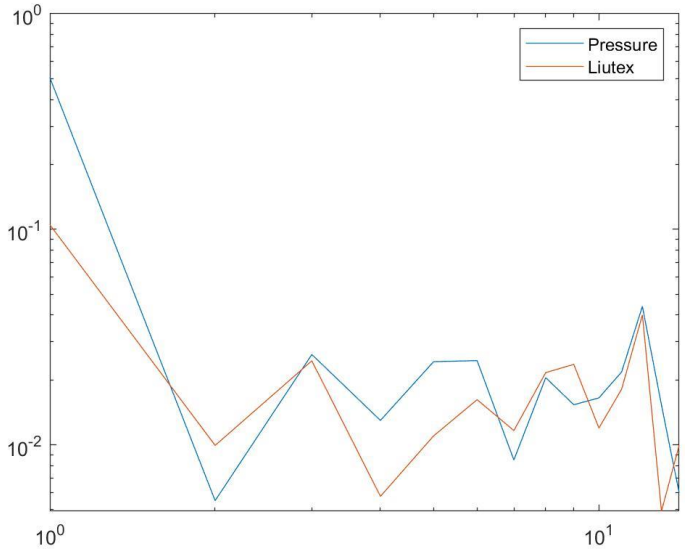

Figure 5.7 7 (j) Power Spectra of Point 10

Figure 5.7. Power spectra of 10 points

5.4 Conclusion

1. An extremely high correlation was observed in the middle and the lower boundary layer positions.
2. The low-frequency noises caused by pressure fluctuation are observed as mainly dominated by the vortex structure or the spectrum of Liutex.
3. The vortex rings are weakened because of the decrease in the pressure gradient between the upstream and downstream of the shock.
4. By the correlation analysis, the pressure fluctuation is closely related to the Liutex. The frequency of pressure fluctuation is the same as the Liutex frequencies.

CHAPTER 6

ANALYSIS ON THE DEVELOPMENT OF LIUTEX, SHEAR, AND VORTICITY IN BOUNDARY LAYER TRANSITION OF FLAT PLATE

6.1 Introduction

The study of vortices, their generation, growth, recognition, and application in fluid dynamics has been well-focused and advanced in applied fields for decades. Hussain [45], highlighted the importance of coherent structures in turbulence, particularly their characteristic measures, coherent vorticity, and helicity. Taylor [46,47] proposed that vortex lines are lengthened and enhanced by random stretching and conservation of circulations in turbulent flows. They also suggested that the stretching of longitudinal vortices induces mixing and dissipation in shear layers. According to Matsumoto and Hoshino's research [48] on the start of turbulence caused by a Kelvin-Helmholtz vortex, the density differential between the two media is a key factor in the rapid mixing and transport of turbulence. A new mechanism of near-wall streamwise vortex production that dominates turbulence phenomena in boundary layers was presented by Schoppa and Hussain [49] in 2002. In their article, they proposed a “shearing” mechanism for creating streamwise vortices, wherein transitory perturbation growth results in the production of a sheet of streamwise vorticity (x), which is then collapsed into streamwise vortices by being stretched by u/x. By using a DNS study on the physics of late boundary layer transition, Liu et al. [16] discussed the mechanism of the large coherent vortex structure formation, small-length scale generation, and flow chaos. They noted that the vorticity rollup and

shear layer instability are required for the flow transition and that the sustenance of turbulence is due to the energy transfer through multiple-level sweeps. According to some researchers, the development, interaction, and annihilation of vortices with a variety of length scales transmit energy in a turbulent flow [50]. Our earlier publications [51-53] made the point that the vorticity (tubes or lines) cannot simply be employed as a signal of the turbulent transition process and cannot directly reflect the vortex. To explain the turbulence generation in late flow transition, the volume Omega Bar (volume) and the volume vorticity [51] were also introduced.

In DNS for the boundary layer flow, due to a periodic boundary condition of the side boundary and a Blasius base flow, the vorticity only has two types of distribution: the self-closed vorticity rings inside the domain, and the unclosed vorticity lines (or tubes) which start from one side boundary S1 and end at the other one S2. Since all vorticity rings that come from a cross-section extracted from the domain normal to spanwise direction must go back to the same one, the total vorticity flux of an arbitrary vorticity ring should be zero. Thus, the total flux of the vorticity over any cross-section parallel to the side boundary remains unchanged: $\int_A \vec{\omega} \cdot \vec{j}\, dA = \int_{s1} \vec{\omega}_y\, dA = \int_{s2} \vec{\omega}_y\, dA$ = const., where dA is the area of any cross-section normal to axis y and $\vec{j}$ denotes the unit vector in the axis y. The computational domain in the streamwise direction is about 40 T-S waves long and the turbulence structures are not properly developed at the initial stage.

For the study, the 25 T-S wave period is selected to analyze the structures in the well-developed turbulent area. Taking the time average of the data at 25 T-S period which roughly includes 55 million grid points is calculated for the components of Vorticity,

Liutex, and Shear. The time average is then used to find the integration of each component at the desired spanwise sections (300-1000).

6.2 Results

Streamwise Sections	$\int_A \omega_x \, dA$	$\int_A \omega_y \, dA$	$\int_A \omega_z \, dA$
300	-1.7×10^{-3}	289.2971	3.5×10^{-3}
400	-4×10^{-3}	289.2971	4×10^{-3}
500	-5.7×10^{-3}	289.2971	1.5×10^{-3}
600	-7.8×10^{-3}	289.2971	-5.9×10^{-3}
700	-7.9×10^{-3}	289.2971	-1.04×10^{-2}
800	-8.7×10^{-3}	289.2971	-1.85×10^{-2}
900	-8×10^{-3}	289.2971	-1.57×10^{-2}
1000	-4.8×10^{-3}	289.2971	-1.01×10^{-2}

Table 6.1 Integral of Vorticity components over the whole domain

The above computation results show that the magnitude of the $\int_A \omega_x \cdot \vec{\imath} \, dA$ and $\int_A \omega_z \cdot \vec{k} \, dA$ has a much smaller order than $\int_A \omega_y \cdot \vec{\jmath} \, dA$, as the spanwise vorticity ω_y is dominant over the whole domain, while the streamwise vorticity ω_x and the normal vorticity ω_z generated by the inflow perturbation are far smaller. Generally, $\int_A \omega_y \cdot \vec{\jmath} \, dA$ does not change with time during the transition in Table 6.1, which shows that the boundary layer transition is not a process with a vorticity increase. Whereas turbulence transition is a process of rotation buildup.

Streamwise Sections	$\int_A R_x \, dA$	$\int_A R_y \, dA$	$\int_A R_z \, dA$
300	8.28×10^{-4}	2.2×10^{-3}	7.35×10^{-4}
400	5.41×10^{-4}	1.51×10^{-2}	1.2×10^{-3}
500	1.8×10^{-3}	2.71×10^{-2}	2.4×10^{-3}
600	7.92×10^{-4}	3.74×10^{-3}	-3.21×10^{-4}
700	2.1×10^{-3}	4.76×10^{-6}	-1.3×10^{-3}
800	-3.8×10^{-3}	6.53×10^{-2}	-7.0×10^{-3}
900	1.5×10^{-4}	8.91×10^{-2}	-4.6×10^{-3}
1000	7.89×10^{-3}	9.95×10^{-2}	-4.4×10^{-3}

Table 6.2 Integral of Liutex components over the whole domain

Streamwise Sections	$\int_A S_x \, dA$	$\int_A S_y \, dA$	$\int_A S_z \, dA$
300	-2.5×10^{-3}	289.2950	2.7×10^{-3}
400	-4.5×10^{-3}	289.2820	2.8×10^{-3}
500	-7.5×10^{-3}	289.2700	-9.4×10^{-4}
600	-8.6×10^{-3}	289.2598	-5.6×10^{-3}
700	$-1.0\times10^{-}$	289.2495	-9.0×10^{-2}
800	-4.8×10^{-3}	289.2318	-1.15×10^{-2}
900	-8.1×10^{-3}	289.2152	-1.11×10^{-2}
1000	-5.6×10^{-3}	289.1977	-5.7×10^{-3}

Table 6.3 Integral of Shear components over the whole domain

According to the vorticity vector decomposition, $\vec{\omega} = \vec{R} + \vec{S}$, where $\vec{R}$ is the Liutex representing the rigid rotation of fluid and $\vec{S}$ represents the anti-symmetric shear part. Based on the

$\vec{R} = \vec{\omega} \cdot \vec{r} - \sqrt{(\vec{\omega} \cdot \vec{r})^2 - 4\lambda_{Ci}^2}$, a comparison of the components at different sections is given in Table 6.2. The integral of the Liutex components increases during the process from an extremely small value. If the vorticity is conserved and the Liutex is increased during the transition, there must be a decrease of $\vec{S}$. Table 6.3 confirms the variation of the integral of the anti-symmetric components.

Moreover, the integral of $\vec{R}$, $\vec{S}$ and $\vec{\omega}$ of the streamwise section is plotted. Clearly, it can be seen that $\int_A \vec{R}\, dA$ increases from zero to large while the $\int_A \vec{S}\, dA$ decreases over time as the results can be seen in Table 6.3. The Liutex and the anti-symmetric shear do not follow the flux conservation law as vorticity does, i.e., $\nabla . \vec{R} \neq 0$ and $\nabla . \vec{S} \neq 0$. Thus, the turbulent transition is the transformation of the anti-symmetric shear to rotation. In addition, the Liutex vector and anti-symmetric shear vector can be the true symbol of the vortex generation.

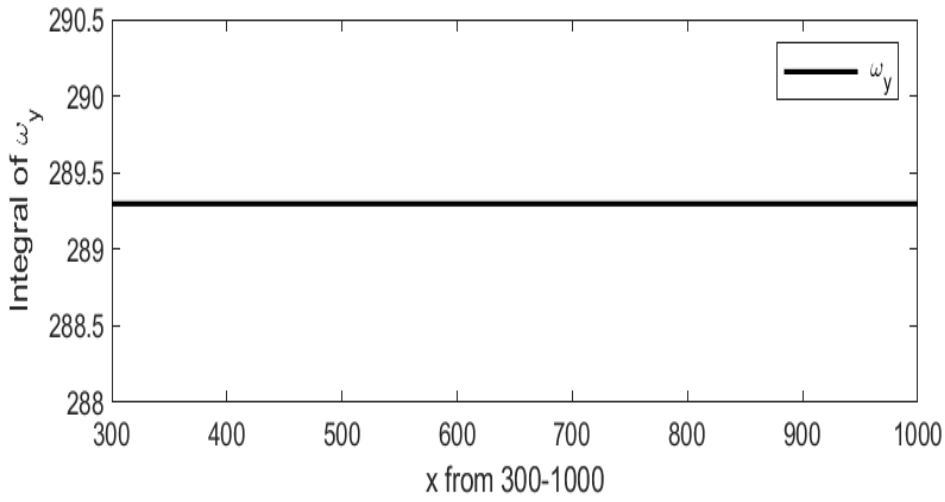

Figure 6.1 (a) Graph of vorticity in the spanwise direction

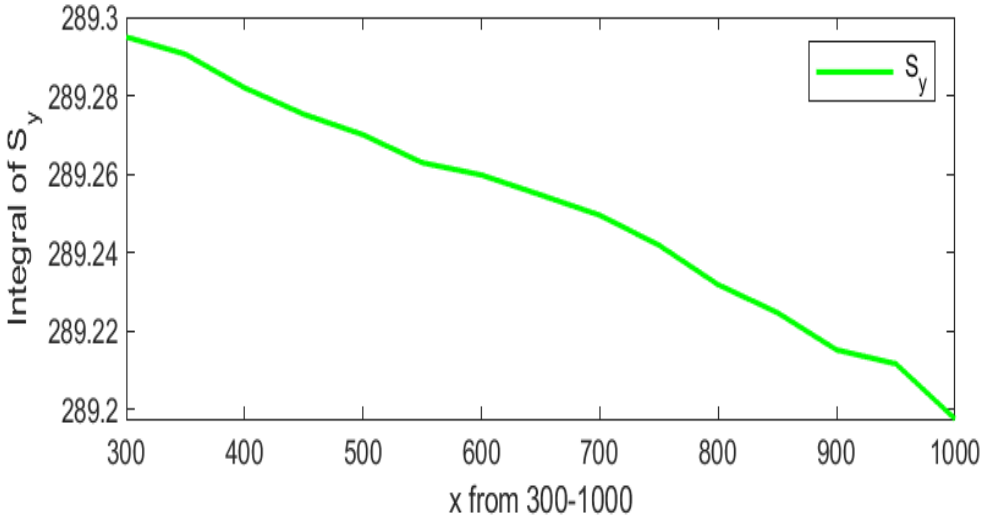

Figure 6.1 (b) Graph of shear in the spanwise direction

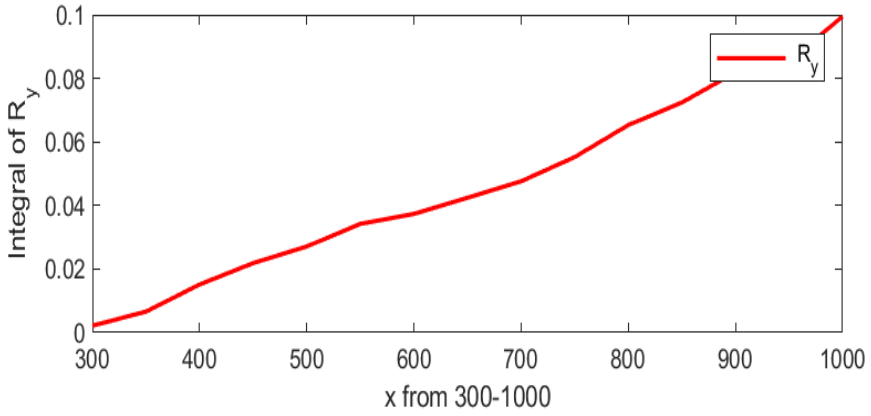

Figure 6.1 (c) Graph of Liutex in the spanwise direction

Figure 6.1 (a)-(c) graphs of Vorticity, Shear, and Liutex in a spanwise direction

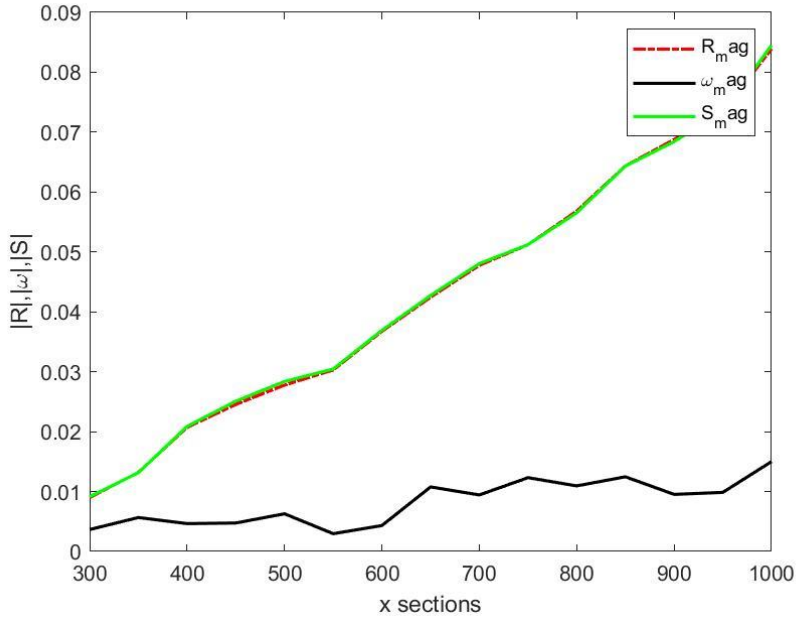

Figure 6.2 Graph of magnitudes of Liutex, Vorticity, and Shear

6.3 Conclusion:

One approach to encourage boundary layer transition is to convert the anti-symmetric shear to rotation, which is in accordance with the mechanism of vortex creation and growth during boundary layer transition. In this regard, the Liutex and the anti-symmetric shear vector are both valuable tools for representing the development and evolution of vortices during this process. While the liutex is a physical parameter that reflects the flow's rotation, it can also be used as a quantitative measure of the transition from laminar to turbulent flow. By analyzing the evolution of the Liutex vector, researchers can predict the onset and intensity of turbulence, allowing them to better understand the underlying and potential applications. Furthermore, it is worth noting that the anti-symmetric shear vector plays a crucial role in determining the location and strength of vortices in boundary layer transition. By analyzing the anti-symmetric shear vector, researchers can gain insight into the mechanics of vortex creation and growth, which can help improve turbulence models and predict flow behavior in practical applications.

CHAPTER 7

LIUTEX-BASED SUBGRID STRESS MODELING

7.1 Subgrid Stress Modeling

One of the commonly used techniques for studying turbulence boundary layers is large-eddy simulation (LES), which can accurately resolve the large-scale structures of turbulent flows and capture the evolution of boundary layer transition. To describe the velocity profile during turbulent boundary layers, popular authors have suggested different models and criteria. For example, in their seminal work, [54] Perry and Chong (1982) proposed a model of the wall turbulence mechanism, which linked the flow visualization with the various quantitative measurements and scaling laws, by using the concept of the horseshoe vortex, hairpin vortex or ‘A’ vortex. They showed a connection between the distribution of the mean velocity, the turbulence intensity distribution, and the turbulence spectrum. In another study, [55] Zaki and Durbin (2005) developed a Reynolds-averaged Navier-Stokes (RANS) based criterion to predict the onset of boundary layer transition, which is based on the maximum value of the turbulence kinetic energy in the streamwise direction. As stated by S. Corrsin and J. L. Lumley [56] in their book, "The Structure of Turbulent Shear Flow," the velocity profile of a turbulent boundary layer is characterized by a logarithmic region in the outer part of the boundary layer, where the velocity varies logarithmically with distance from the wall. This logarithmic region is a hallmark of turbulent boundary layers and is crucial in understanding the mechanism of turbulence. Moreover, in their paper "The Law of the Wall in Turbulent Shear Flow," J. Nikuradse and

R. von Kármán [57] showed that the velocity profile of a turbulent boundary layer obeys a power law, known as the "law of the wall." This law relates the velocity to the distance from the wall and the viscosity of the fluid and has been widely used in the modeling of boundary layer flows. In the LES of the turbulence boundary layer, the velocity profile plays a crucial role in the subgrid-scale modeling of the turbulent structures. Therefore, the accurate characterization and modeling of the velocity profile in the boundary layer is essential for understanding the transition process and for the development of accurate LES models.

In the current work, we aim to investigate the velocity profile during the turbulence boundary layer using LES and compare the results with the Smagorinsky model. This will provide insights into the underlying mechanisms of boundary layer transition and contribute to the development of more accurate and reliable prediction models for practical applications.

7.1.1 Smagorinsky Model:

The Smagorinsky model is one of the first introduced and most widely used LES sub-grid stress models. The model was proposed by Joseph Smagorinsky in 1963. It is based on the concept of eddy viscosity, where the unresolved turbulent eddy effects are represented by an additional viscosity term in the governing equations. This additional term works as a diffusive process to account for the energy transfer from the resolved large-scale eddies to the unresolved small-scale eddies. The linear relation between the eddy viscosity and the magnitude of large-scale deformation tensor in the following form

$$v_t = C_s \Delta^2 \bar{S} = C_s \Delta^2 \sqrt{2 \bar{S}_{ij} \bar{S}_{ij}} \tag{7.1}$$

Where, v_t is the eddy viscosity,

C_s is a model coefficient,

Δ is a characteristic length scale often determined by the filtering width of the mesh $\Delta = (\Delta_x \Delta_y \Delta_z)^{\frac{1}{3}}$, and $\bar{S}_{ij} = \frac{1}{2}\left(\frac{\partial \overline{u_i}}{\partial x_j} + \frac{\partial \bar{u}_j}{\partial x_i}\right)$ represents the filtered rate-of-strain tensor.

The model coefficient has different suggested values, but it usually adopts a 0.1-0.2 value. Even though the model is simple and well-known there is one drawback of the Smagorinsky model, that is it overestimates the eddy viscosity under strong background shear. It leads to a non-zero residual viscosity and shear stress at the wall.

7.1.2 WALE Model

Another well-known subgrid stress model is the Wall-Adopting Local Eddy-viscosity model commonly known as WALE used in LES to capture turbulent vortex structures in engineering and complex flow simulations. Like Smagorinsky, the WALE model is also based on the eddy-viscosity concept, but it is more accurate and incorporates dynamic estimation of the eddy viscosity that adapts to the local flow conditions. This behavior makes the WALE model more suitable for flows with strong shear and rotational effects. Proposed by Nicoud and Ducros in 1999 as an extension of the Smagorinsky model.

$$v_t = \rho \Delta_s^2 \ \frac{(S_{ij}^d S_{ij}^d)^{3/2}}{(\bar{S}_{ij} \bar{S}_{ij})^{5/2} + (S_{ij}^d S_{ij}^d)^{5/4}} \tag{7.2}$$

$$\Delta_s = C_w V^{\frac{1}{3}}, \tag{7.3}$$

$$S_{ij}^d = \frac{1}{2}(\bar{g}_{ij}^2 + \bar{g}_{ij}^2) - \frac{1}{3}\delta_{ij}\bar{g}_{kk}^2 \tag{7.4}$$

$$\bar{g}_{ij}^2 = \bar{g}_{ik}\bar{g}_{kj}, \tag{7.5}$$

$\bar{g}_{ij} = \frac{\partial \bar{u}_i}{\partial x_j}$ is the operator added based on the traceless symmetric part of the square of the velocity gradient tensor and $\bar{S}_{ij} = \frac{1}{2}\left(\frac{\partial \bar{u}_i}{\partial x_j} + \frac{\partial \bar{u}_j}{\partial x_i}\right)$ is the strain rate tensor.

The most used WALE model constant is $C_w = 0.55 - 0.60$.

Improves the prediction of sub-grid-scale turbulence, particularly in wall-bounded flows, where resolving the near-wall region can be computationally expensive.

7.1.3 Wang's Liutex-Based Model

The Liutex-based subgrid stress model is based on the third-generation vortex identification-based method that is Liutex. It was proposed by Wang et al. in 2023, to overcome the issues with the WALE and Smagorinsky model. As we all know, Smagorinsky over-predicts the eddy viscosity and so WALE was introduced which solved the over-prediction issues, but it is too complicated. Whereas the Liutex-based model does not deal with any such issues, in fact, it is not even affected by shear.

The model is expressed as follows:

$$v_t = C_v \Delta^2 \overline{\mathrm{R}}, \tag{7.6}$$

Where the Δ-filtering length scale is defined as $\Delta = (\Delta_x \Delta_y \Delta_z)^{\frac{1}{3}}$,

$$\overline{\mathrm{R}} = \sqrt{\overline{\mathrm{R}}_1^2 + \overline{\mathrm{R}}_2^2 + \overline{\mathrm{R}}_3^2} \tag{7.7}$$

Where $\overline{\mathrm{R}}$ is the filtered Liutex magnitude

The constant $C_v = 0.032$.

In the following, we will test this new Wang's model in two LES cases, a coarse grid 960*64*121 and a coarse grid 960*32*61 of the turbulent flat plate flow. The Log Law is implemented to check the mean velocity profile of the turbulent boundary layer.

7.2 Law of the Wall

The law of the wall, also popularly known as the logarithmic law of the wall states that the average velocity of a turbulent flow at a certain point is proportional to the logarithm of the distance from the wall, Theodore von Karman.

$$u^+ = \frac{1}{k} ln\, z^+ + c^+, \tag{7.8}$$

$$\text{with } z^+ = \frac{z u_\tau}{\nu} \tag{7.9}$$

$$u_\tau = \sqrt{\frac{\tau_w}{\rho}} \text{ and} \tag{7.10}$$

$$u^+ = \frac{u}{u_\tau} \tag{7.11}$$

Where,

z^+- dimensionless wall coordinate

u^+- dimensionless velocity

τ_w- wall shear stress

ρ- fluid density

u_τ- shear velocity

k- Von Karman constant

c^+- a constant

In the research the k, c^+ value is approximately 0.41 and 5.0, respectively. In Figures 3 and 4, we show the time and spanwise-averaged velocity profile, plotted in terms of logarithm scaled wall unit. The curves of the linear law and the log law are also plotted for comparison. For the DNS case, the viscous sublayer region is found to be $z^+ < 7^+$, whereas the buffer layer is between 7 and 30 wall units. In this region, $u^+ \neq z^+$, and $u^+ \neq \frac{1}{k} ln\, z^+ + c^+$. After 30 wall units, the logarithmic law is used at the fully developed turbulent zone.

Time and spanwise averaged streamwise velocity profiles for various streamwise locations in two different grids are shown. At x=600δ_{in}, the mean velocity profile approaches a turbulent flow velocity profile that is Log Law. This comparison shows that the velocity profile from the DNS results in a turbulent flow velocity profile and the grid convergence has been realized.

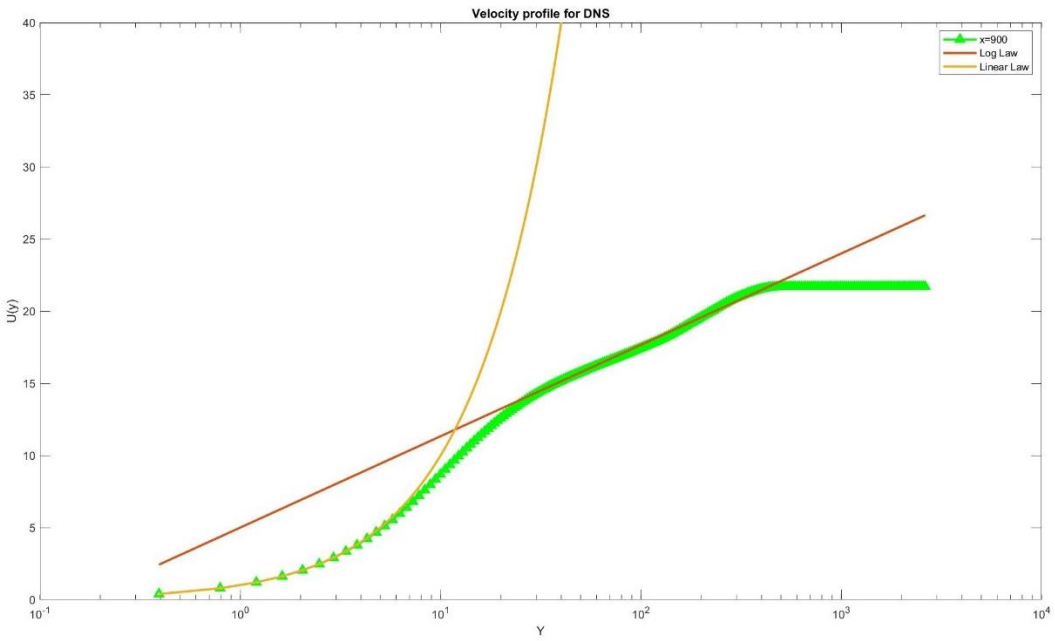

Figure 7.1 Log profile of DNS flat plate

The mean velocity profile results in figure 7.2 is given by [58] H. Abe, H. Kawamura, Y. Mastuo for the turbulent channel flow proves that our DNS velocity profile for the flat plate agrees with the Von Karman law.

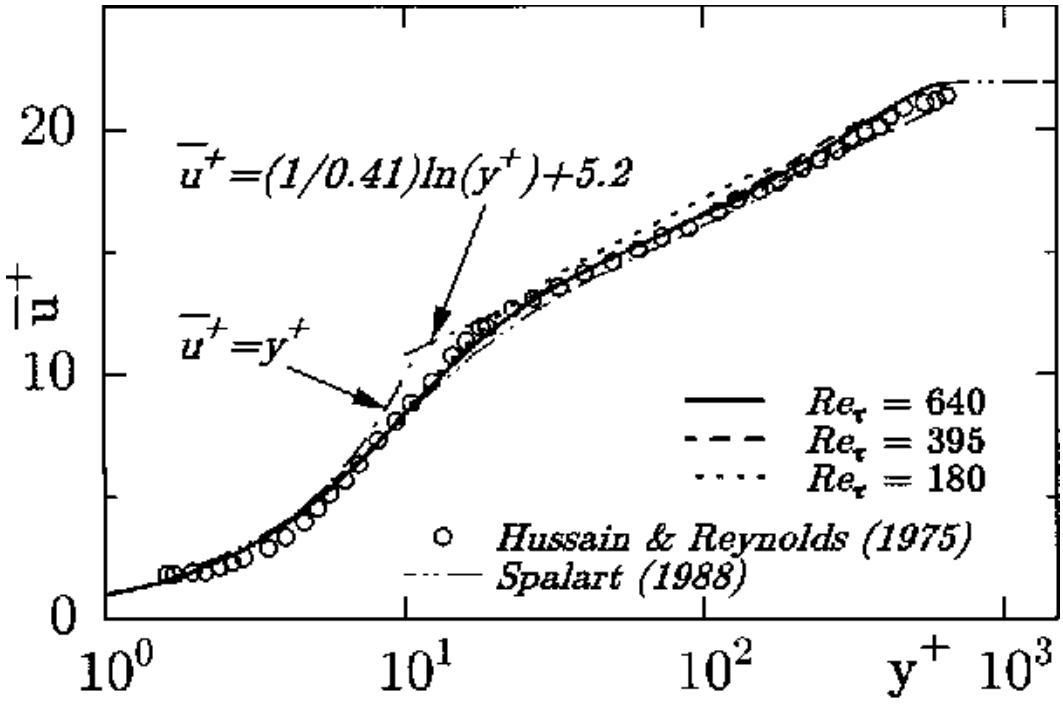

Figure 7.2 Mean velocity profile by H. Abe, H. Kawamura, Y. Mastuo

7.3 Skin Friction Coefficient

The figure illustrates the skin friction coefficient results obtained from the time and spanwise average velocity profile. For comparison, we also consider the spatial evolution of the skin friction coefficient in laminar flow. Notably, the graph highlights a significant increase in the skin friction coefficient after $x \approx 450\delta_{in}$, where $Re_x = 5.0 \times 10^6$, defining the transition point. Beyond this transition stage, the friction

coefficient aligns well with the theoretical expectations for the turbulent boundary layer on a flat plate.

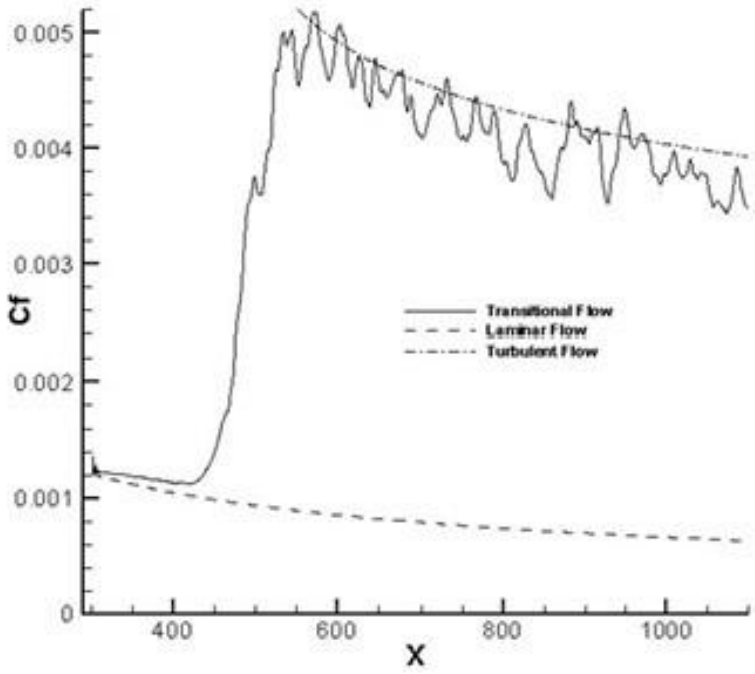

Figure 7.3 Time and spanwise average skin friction coefficient

7.4 Results

7.4.1 Case -I: LES 960*64*121

The following is the time and spanwise average of the mean velocity profile at different streamwise locations. The grids are 8 times more coarse than DNS. The Von Karman constants are k=2.75 and C=5.2. At $x = 600\delta_{in}$, the mean velocity profile has reached the turbulent flow velocity profile. Figure 7.4 (a-b) presents the time and spanwise averaged velocity profile, represented using a logarithmic scale in wall units. Additionally, we have included curves representing the linear law in the near-wall region and the log law for comparison. The green curve is the DNS profile, the black

curve is the no model LES curve, the blue curve is the modeled, and the purple is the Smagorinsky modeled curve.

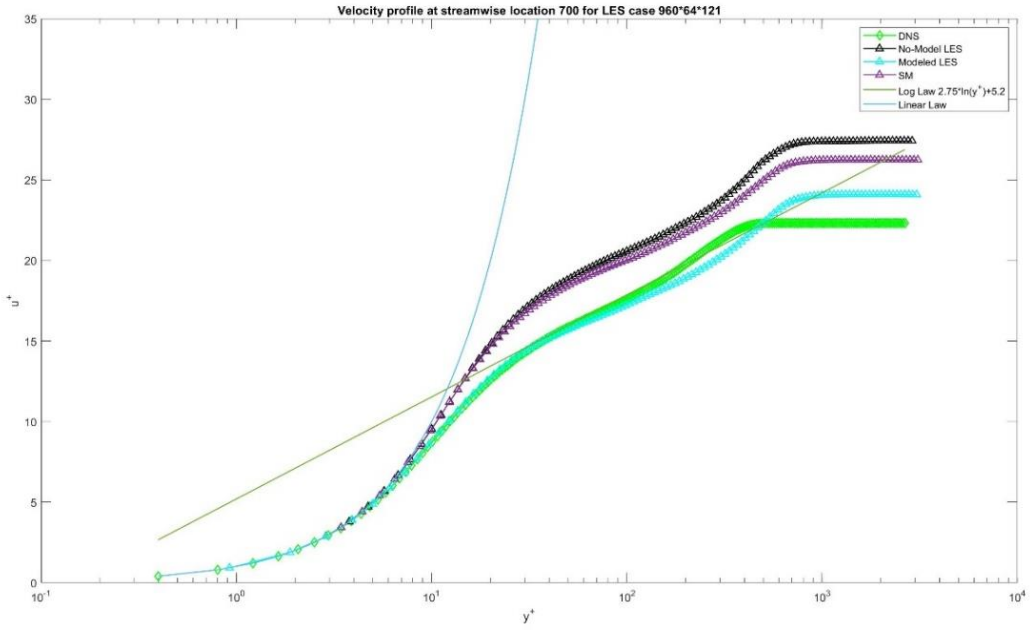

Figure 7.4 (a) Log profile at streamwise location x=700

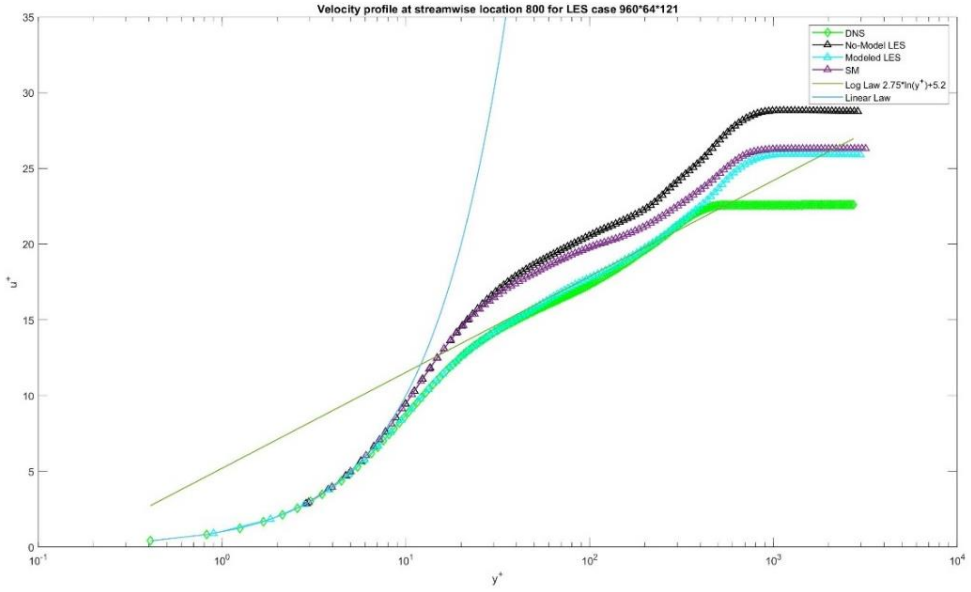

Figure 7. 4 (b) Log profile at streamwise location x=800

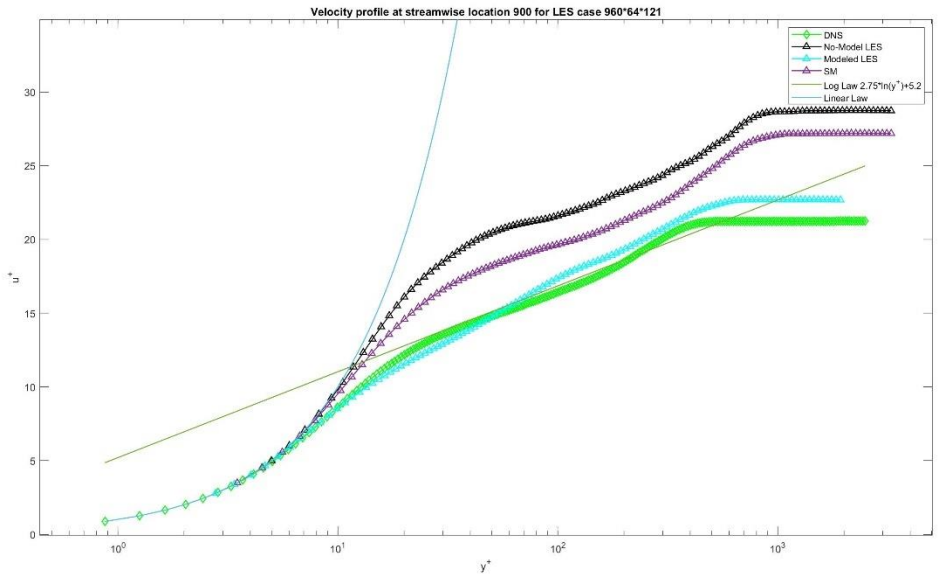

Figure 7. 4 (c) Log profile at streamwise location x=900

The logarithmic profile exhibits encouraging results, demonstrating the convergence of the Liutex-based model towards the DNS curve.

7.4.2 Case-II: LES 960*32*61

Figure 7.5 (a-b) presents the time and spanwise averaged velocity profile, represented using a logarithmic scale in wall units. Additionally, we have included curves representing the linear law in the near-wall region and the log law for comparison.

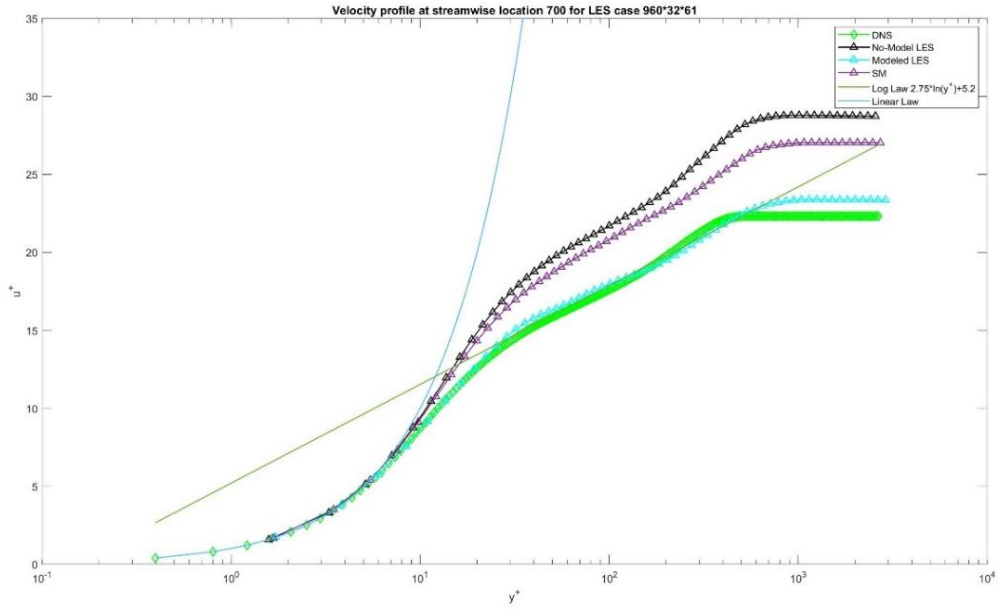

Figure 7. 5 (a) Log profile at streamwise location x=700

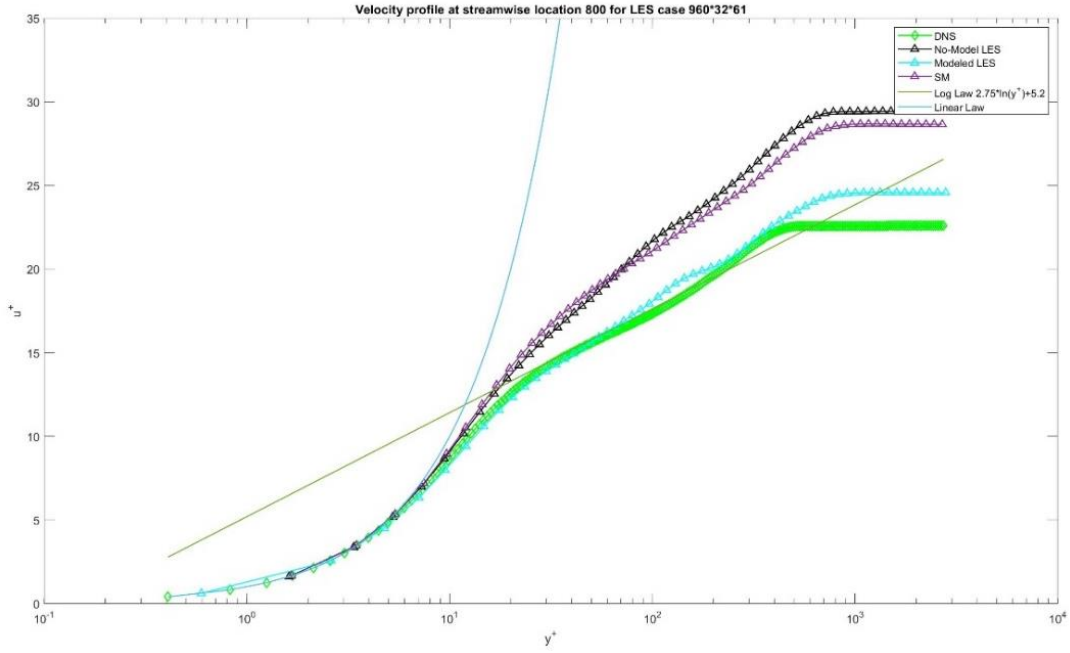

Figure 7. 5 (b) Log profile at streamwise location x=800

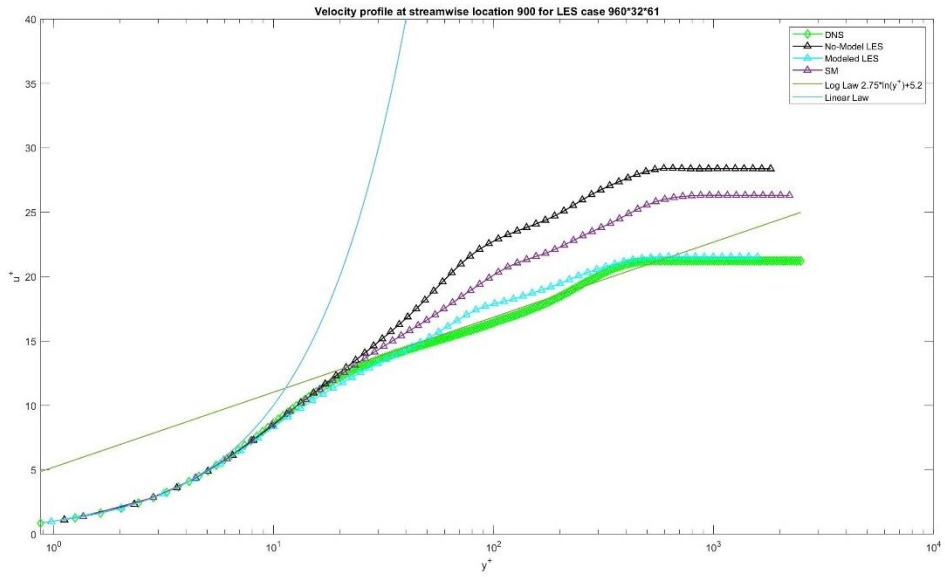

Figure 7. 5 (c) Log profile at streamwise location x=900

The log profile shows the promising results of the convergence of the Liutex-based model to the DNS curve.

7.4.3 Streamwise velocity profile

Figure 7.6 (a-f) displays the time and spanwise averaged streamwise velocity profiles at different streamwise locations, starting from x=550δ_{in}, where δ_{in} represents the inner boundary layer thickness. The mean velocity profile in this region exhibits characteristics of turbulent flow. Additionally, we have included LES cases I and II to examine the flow behavior in the turbulent boundary layer. A clear comparison of the results reveals that the Smagorinsky model fails to accurately match the DNS curve in the turbulent region. On the other hand, the LES Liutex-Based model demonstrates promising

results, proving its superiority in capturing the behavior of the flat plate turbulent boundary layer case.

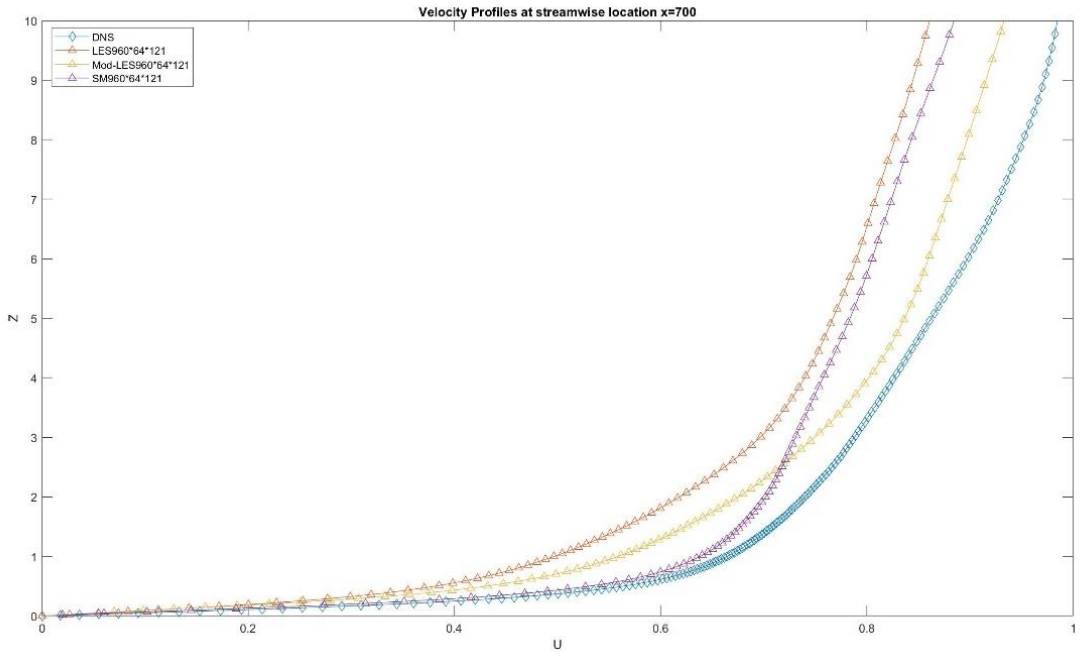

*Figure 7. 6 (a) Case I 960*64*121 at x=700*

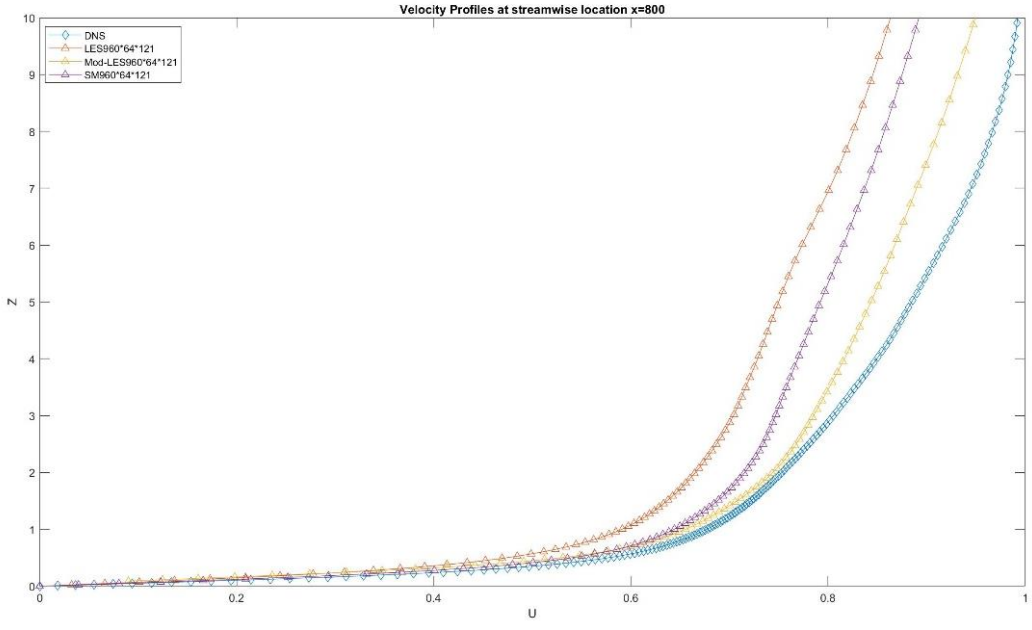

*Figure 7. 6 (b) Case I 960*64*121 at x=800*

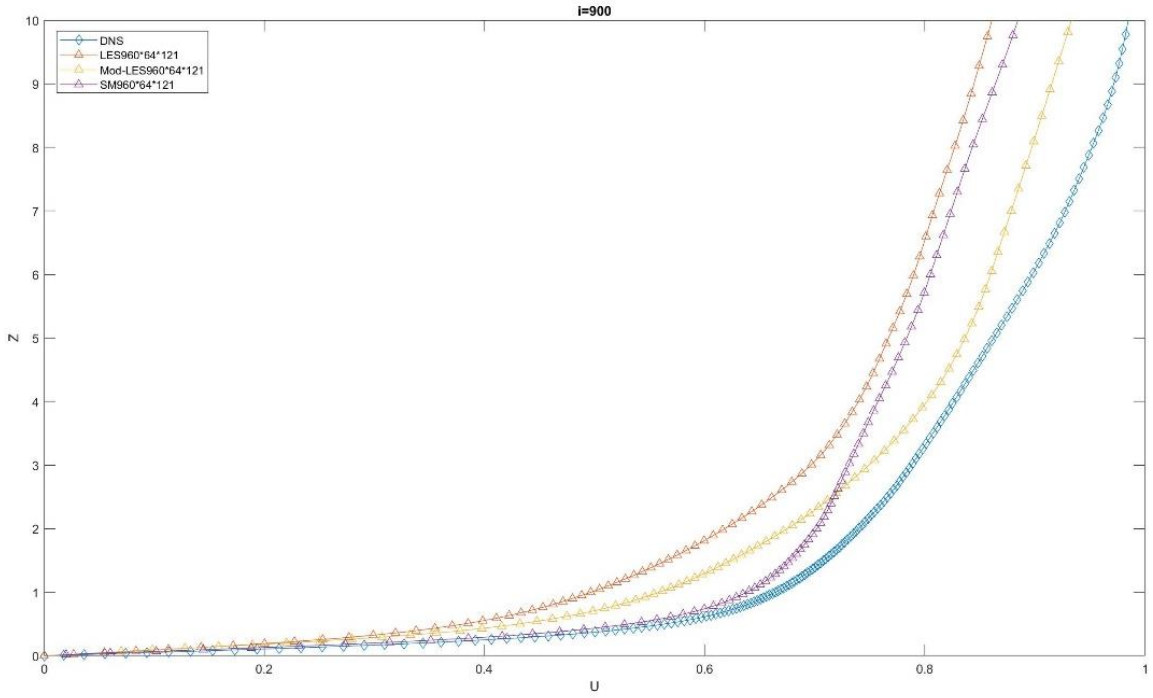

*Figure 7. 6 (c) Case I 960*64*121 at x=900*

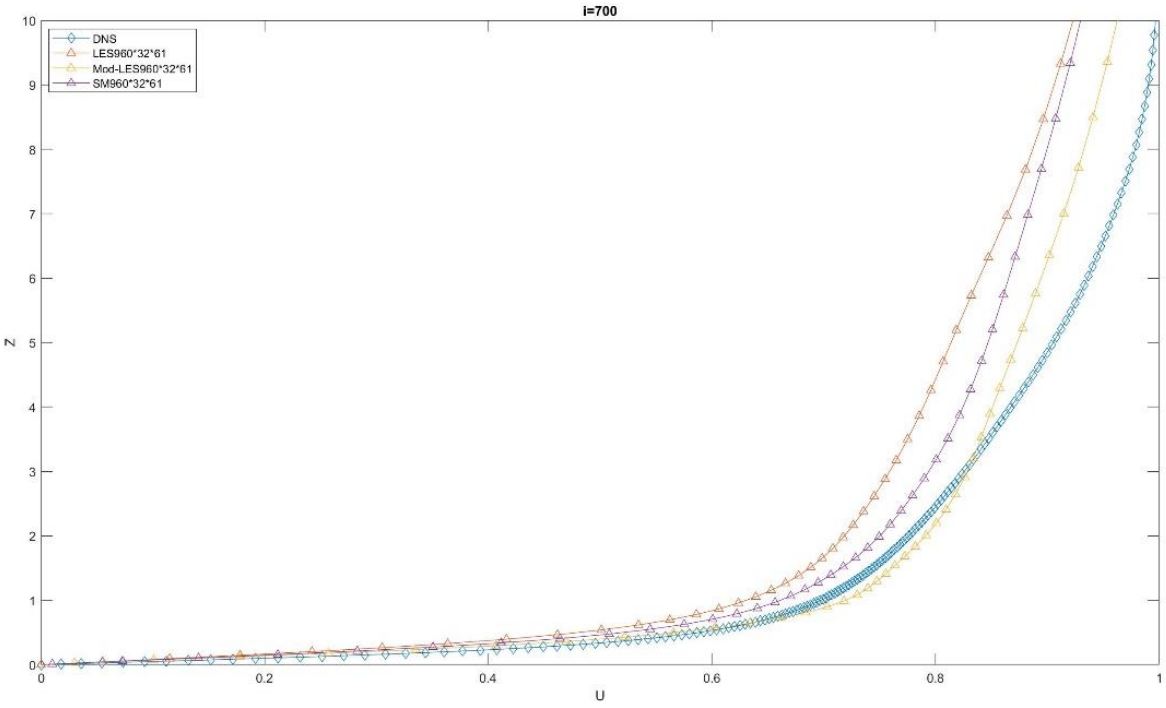

*Figure 7. 6 (d) Case II 960*32*61 at x=700*

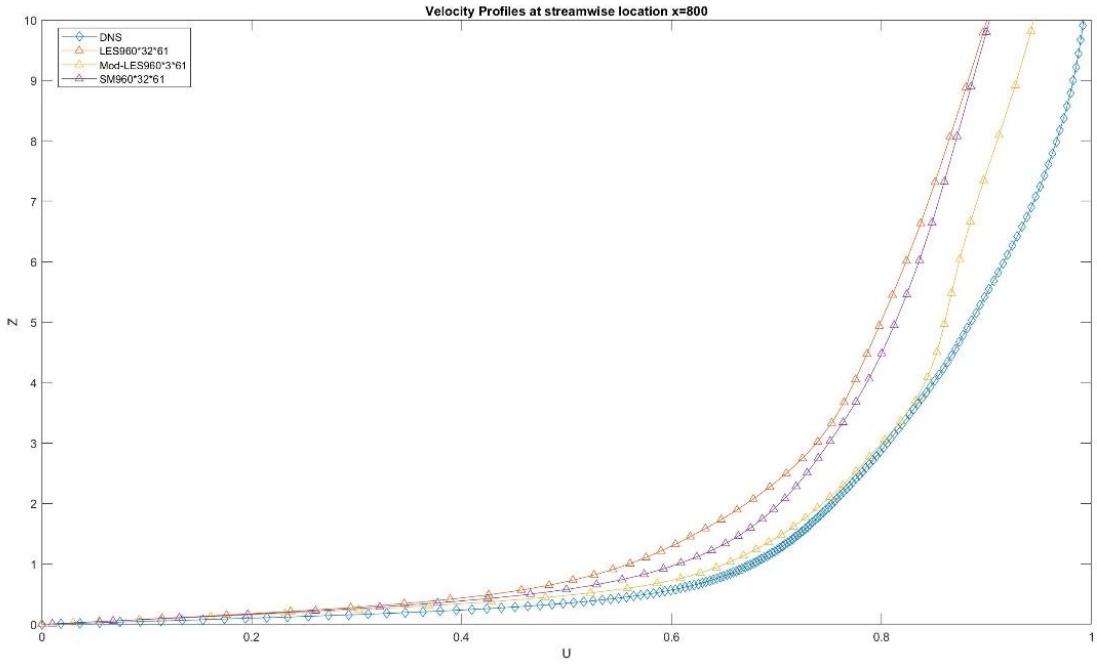

*Figure 7.6 (e) Case II 960*32*61 at x=800*

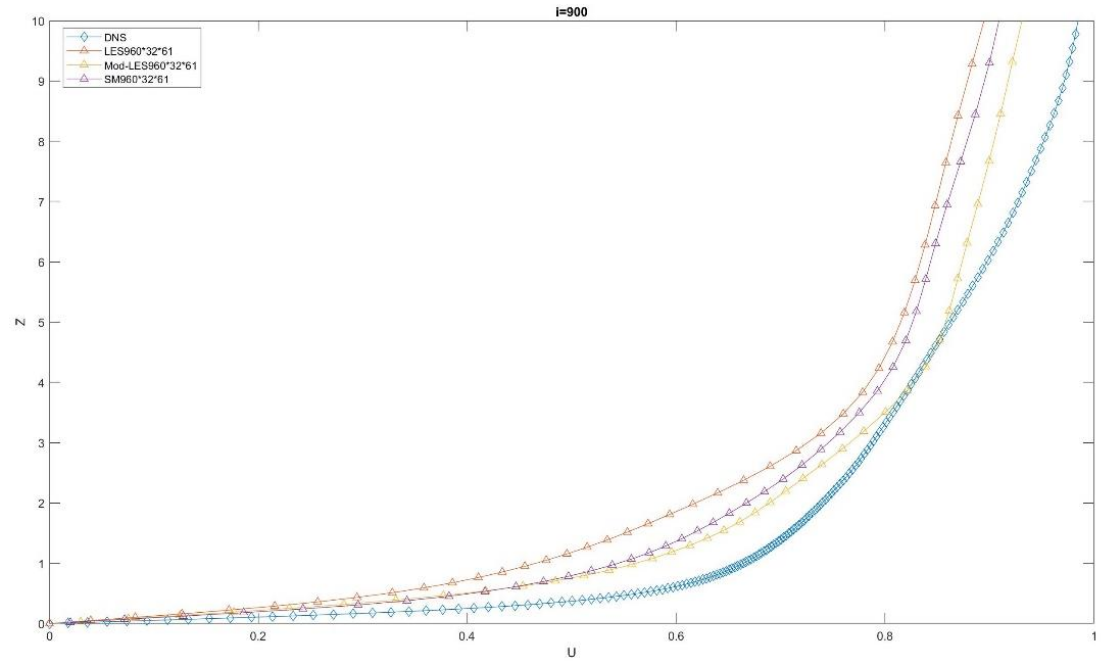

*Figure 7. 6 (f) Case II 960*32*61 at x=900*

7.5 Computation

The TACC Stampede 2 machine has been employed for simulations, particularly in cases involving the Direct Numerical Simulation (DNS) approach. For scenarios with around 60 million grid points, DNS necessitates a computational timeframe of approximately two weeks to achieve a turbulent flow stage. In contrast, the Large Eddy Simulation (LES) technique proves more efficient. In LES, a case with 7 million grid points is computed within a single day, while a scenario with approximately 1 million grid points is resolved in just seven hours.

In the realm of engineering applications, such as aircraft and large ships, where simulations demand trillions of grid points, completion may span several months. Given the accuracy achieved by LES utilizing subgrid stress models, a pertinent question arises: why not favor LES over DNS? While not every small vortex structure is directly resolved in LES modeling, the speed of computation becomes a pivotal factor. Opting for a method that delivers results in a matter of days significantly outweighs waiting months for completion.

In essence, LES with subgrid stress modeling emerges as a highly dependable method. It provides an optimal balance between resolving critical flow features and expediting computational efficiency. This renders LES an indispensable choice for addressing intricate engineering challenges, ensuring accurate results without compromising the timeframe.

7.6 Conclusion

The comparative analysis of two different test cases for Large Eddy Simulation (LES) on a flat plate reveals that Wang's Liutex-based model outperforms other models. The regular velocity and wall-normal graphs demonstrate that Wang's model exhibits excellent agreement with the well-known Von Karman law. The efficiency and accuracy of the Liutex-based model are evident in the analysis of the turbulent boundary layer, where it outperforms the Smagorinsky model without any overprediction issues.

One of the key advantages of using Wang's Liutex-based model is its efficiency compared to the Smagorinsky model. Additionally, it avoids overprediction, a common limitation of the Smagorinsky model. Moreover, the Liutex-based model is uniquely equipped with vortex identification capabilities, setting it apart from the WALE and Smagorinsky models.

The formula used in the Liutex-based subgrid stress model strikes a balance between simplicity and accuracy, making it more straightforward than the WALE model while avoiding the complexity associated with WALE. This simplicity in the Liutex-based model ensures ease of implementation and computational efficiency.

Another significant distinction lies in the treatment of eddy viscosity near the wall. The Smagorinsky model does not enforce zero eddy viscosity at the wall, resulting in non-zero values, whereas the WALE model sets the eddy viscosity at around 0.1v (where v is the kinematic viscosity). On the other hand, the Liutex-based model strictly maintains zero eddy viscosity at the wall boundary, making it more suitable for wall-bounded flows and boundary layer simulations.

The model constant (C_w) for the Liutex-based model is determined to be 0.032, which has shown to be reliable for both the flat plate case and turbulent channel flow, surpassing the performance of the constants used in other models.

In conclusion, Wang's Liutex-based model demonstrates its superiority over other tested models in the context of LES on a flat plate. It achieves good agreement with the Von Karman law, exhibits high efficiency, and avoids overprediction issues. With the added advantage of being a vortex identification method, the Liutex-based model provides valuable insights into the complex dynamics of turbulent flows. Its straightforward formula and the enforcement of zero eddy viscosity at the wall make it a robust choice for simulating wall-bounded flows and boundary layer transitions.

CHAPTER 8

SUMMARY

The three generations of vortex identification techniques have, in my opinion, significantly advanced our knowledge of turbulent flows. Among these, the third-generation approach, Liutex, has become a potent instrument that gets around the drawbacks of its forerunners. Liutex excels in modeling subgrid stress because it takes a vector form and is unaffected by shear. This makes it a desirable tool for Large Eddy Simulation (LES) studies.

Liutex has been used to simulate Supersonic Ramp Flow with or without Multiple Vortex Generators (MVG), and the results are remarkable. The association between low-frequency distributions and shock oscillations has been revealed by a detailed investigation of various Mach numbers. Notably, strong relationships between pressure variations and low-frequency vortices were discovered, providing information on how to reduce shock-induced flow separation noise by reducing Liutex frequencies.

Beyond its use in LES simulations, Liutex is significant in other contexts. It is a useful tool for showing how vortices grow and change, making it possible to predict when turbulence will start to occur and how intense it will be. A wide range of prospective technical applications are made possible by this improved understanding of underlying dynamics. Liutex's discovery of the anti-symmetric shear vector is particularly helpful in pinpointing the position and intensity of vortices within boundary layers. Such knowledge

enables turbulence model advancements and makes precise flow behavior prediction in engineering applications possible.

Furthermore, the ground-breaking Wang's Liutex-based model has demonstrated its advantage over competing theories. Our knowledge of turbulent flows in engineering applications has increased because of the novel vortex detection approach. Furthermore, LES has become the go-to computational technique, demonstrating its benefits over DNS and RANS in terms of computational effectiveness and simplicity of use. The precise and economical results from flat plate simulations further support Liutex's potential for engineering applications.

In conclusion, using Liutex and adopting LES have changed how we approach researching turbulent flows. Our understanding of the dynamics of fluid systems has increased because of our capacity to control the complexity of vortices. These developments have improved engineering designs, improved turbulence prediction, and optimized performance across numerous industries. It is impossible to overestimate the importance of LES and Liutex-based modeling since they open the door to more sophisticated and effective fluid dynamics solutions and a new era of engineering applications.

REFERENCES

[1] Liu J., Gao Y., Liu C. An objective version of the Rortex vector for vortex identification [J]. *Physics of Fluids*, 2019, 31(6): 065112.

[2] Dong X., Gao Y., Liu C. New normalized Rortex/vortex identification method [J]. *Physics of Fluids*, 2019, 31(1): 011701.

[3] Liu J., Liu C. Modified normalized Rortex/vortex identification method [J]. *Physics of Fluids*, 2019, 31(6): 061704.

[4] Gao Y. S., Liu J. M., Yu Y. et al. A Liutex-based definition and identification of vortex core center lines [J]. *Journal of Hydrodynamics*, 2019, 31(3): 445-454.

[5] Xu H., Cai X. S., Liu C. Liutex (vortex) core definition and automatic identification for turbulence vortex structures [J]. *Journal of Hydrodynamics*, 2019, 31(5):857-863.

[6] Liu C., Gao Y., Tian S. et al. Rortex-A new vortex vector definition and vorticity tensor and vector decompositions [J]. *Physics of Fluids*, 2018, 30(3): 035103.

[7] Pope, S.B. (2000) Turbulent flows. Cambridge University Press.

[8] Germano, M., Piomelli, U., Moin, P., & Cabot, W. H. (1991). A dynamic subgrid-scale eddy viscosity model. Physics of Fluids A: Fluid Dynamics, 3(7), 1760-1765.

[9] Nicoud, F., & Ducros, F. (1999). Subgrid-scale stress modeling based on the square of the velocity gradient tensor. Flow, turbulence and combustion, 62(3), 183-200.

[10] Ding, Y., Pang, By., Yan, Bw., Y. Wang *et al.* A Liutex-based subgrid stress model for large-eddy simulation. *J Hydrodyn* **34**, 1145–1150 (2022).

[11] Smagorinsky J. General circulation experiments with the primitive equations: I. The basic equations [J]. *Monthly Weather Review*, 1963, 91: 99-164.

[12] L. Chen, X. Liu, M. Oliveira, and C. Liu (2010), DNS for late-stage structure of flow transition on a flat-plate boundary layer, in the 48th AIAA Aerospace Sciences Meeting Including the New Horizons Forum and Aerospace Exposition

[13] P. Lu, Z. Wang, L. Chen, and C. Liu (2012). "Numerical study on U-shaped vortex formation in late boundary layer transition," Computers & fluids 55, 36-47

[14] L. Jiang, C.-L. Chang, M. Choudhari, and C. Liu (2003), Cross-validation of DNS and PSE results for instability-wave propagation in compressible boundary layers past curvilinear surfaces, in the 16th AIAA Computational Fluid Dynamics Conference

[15] L. Jiang, C.-L. Chang, M. Choudhari, and C. Liu (2003), Cross-validation of DNS and PSE results for instability-wave propagation in compressible boundary layers past curvilinear surfaces, in the 16th AIAA Computational Fluid Dynamics Conference.

[16] Liu, C., Yan, Y., and Lu, P., "Physics of turbulence generation and sustenance in a boundary layer," Computers & Fluids, Vol. 102, 2014, pp. 353-384.

[17] Yan, Y., Chen, C., Huankun, F., and Liu, C., "DNS study on K-vortex and vortex ring formation in flow transition at Mach number 0.5," J. Turbulence, Vol. 15, No. 1, 2014, pp. 1-21.

[18] Chen, L., and Liu, C., "Numerical study on mechanisms of second sweep and positive spikes in transitional flow on a flat plate," J. Comput. Fluids, Vol.40, 2011, pp. 28–41.

[19] Bake, S., Meyer, D., and Rist, U., "Turbulence mechanism in Klebanoff transition: a quantitative comparison of experiment and direct numerical simulation," J. Fluid Mech., Vol. 459, 2002, pp. 217-243.

[20] Lee, C. B., and Li, R. Q., "A dominant structure in turbulent production of boundary layer transition," J. Turbul., Vol. 8,2007, 55

[21] Hunt, J. C., Wray, A. A., and Moin, P., “Eddies, Streams, and Convergence Zones in Turbulent Flows”, Center for Turbulence Research: Proceedings of the Summer Program, N89-24555 (1988).

[22] Jeong, J., and Hussain F., “On the identification of a vortex,” J. Fluid Mechanics, Vol. 285, 1995, pp. 69-94.

[23] Wang Y., Yang Y., Yang G. et al. DNS study on vortex and vorticity in late boundary layer transition [J]. *Communications in Computational Physics*, 2017, 22(2): 441-459.

[24] J. Liu, Y. Deng, Y. Gao, S. Charkrit, C. Liu, Mathematical foundation of turbulence generation from symmetric to asymmetric Liutex, Journal of Hydrodynamics, 2019, 31(3): 632-636.

[25] Liu, C., Gao, Y., Dong X., Wang, Y., Liu, J., Zhang, Y., Cai, X., and Gui, N., “Third generation of vortex identification methods: Omega and Liutex/Rortex based systems”, *Journal of Hydrodynamics*, 31(2): 205-223 (2019).

[26] Gao Y., Liu C. Rortex and comparison with eigenvalue based vortex identification criteria [J]. *Physics of Fluids*, 2018, 30: 085107.

[27] Wang Y., Gao Y., Liu C. Physical meaning of vorticity based on the Liutex-shear decomposition and explicit formula for the Liutex vector [J]. arXiv:1812.10672 (also submitted to Physics of Fluids).

[28] Liu, J., and Liu, C., “Modified normalized Rortex/vortex identification method,” Physics Fluids, Vol. 31 (6), 2019, 061704.

[29] Dolling, D.S., “Fifty years of shockwave/boundary-layer interaction research: what next?” AIAA J., Vol. 39, pp. 1517–1531, 2001

[30] Delery J, Marvin J. Shock-Wave Boundary Layer Interactions. AGARDograph 280. Brussels: NATO,1986.

[31] Dolling DS. Fluctuating loads in shock-wave/boundary-layer interaction: tutorial and update. Presented at AIAA Aerosp. Sci. Meet. Exhib., 31st, Reno, NV, AIAA Pap. 1993-028

[32] Smits, A.J. and Dussauge, J.-P., Turbulent Shear Flow in Supersonic Flow, Springer, New York, 2006.

[33] Andreopoulos Y, Agui JH, Briassulis G. Shock wave-turbulence interactions. Annu. Rev. Fluid Mech. 32:309–45, 2000.

[34] Lee S, Goetzke MK, Loth E, Tinapple J, Benek J. Microramps upstream of an oblique shock/boundary-layer interaction. AIAA J 48(1):104–118, 2010.

[35] Zheltovodov A. Shock wave/turbulent boundary layer interactions: fundamental studies and applications. Presented at AIAA Fluid Dyn. Conf., 27th, New Orleans, AIAA Pap. 1996-1977

[36] Clemens, Narayanaswamy. Low-frequency unsteadiness of shock wave/turbulent boundary layer interactions. Annu. Rev. Fluid Mech. 46: 469-492, 2014.

[37] Erengil ME, Dolling DS. Physical causes of separation shock unsteadiness in shock wave turbulent boundary layer interactions. Presented at AIAA Fluid Dyn. Conf., 24th, Orlando, FL, AIAA Pap. 1993-3134

[38] Erengil ME, Dolling DS. Effects of sweepback on unsteady separation in Mach 5 compression ramp interactions. AIAA J. 31:302–11, 1993.

[39] Unalmis OH, Dolling DS. Decay of wall pressure field structure of a Mach 5 adiabatic turbulent boundary layer. Presented at AIAA Fluid Dyn. Conf., 25th, Colorado Springs, AIAA Paper. 1994-2363, 1994.

[40] Ganapathisubramani B, Clemens NT, DollingD. Low-frequency dynamics of shock-induced separation in a compression ramp interaction J. Fluid Mech. 636:397–436, 2009.

[41] R. A. Humble, G. E. Elsinga, F. Scarano, and B. W. V. Oudheusden, "Three-dimensional instantaneous structure of a shock wave/turbulent boundary layer interaction," J. Fluid Mech. 622, 33, 2009.

[42] Dupont P, Haddad C, Ardissone JP, Debi`eve JF. Space and time organization of a shock wave/turbulent boundary layer interaction. Aerospace Sci. Technol. 9:561–72, 2005.

[43] S. Priebe and M. P. Martín, "Low-frequency unsteadiness in shock wave turbulent boundary layer interaction," J. Fluid Mech. 699, 1,2012.

[44] X. Dong, Y. Yan, Y. Yang G. Dong, C. Liu, Spectrum study on unsteadiness of shock wave-vortex ring interaction, Physics of Fluids, 2018, 30(5): 056101.

[45] Hussain AF. Coherent structures and turbulence. J Fluid Mech 1986;173:303–56.

[46] Taylor GI. The statistical theory of isotropic turbulence. J Aeronaut Sci 1937;4(8): 311–5.

[47] Taylor GI. Production and dissipation of vorticity in a turbulent fluid. Proc R Soc Lond Ser A-Math Phys Sci 1938;164(916):15–23.

[48] Matsumoto Y, Hoshino M. Onset of turbulence induced by a Kelvin-Helmholtz vortex. Geophys Res Lett 2004;31(2)[49] Schoppa W, Hussain F. Coherent structure generation in near-wall turbulence. J Fluid Mech 2002;453:57–108.

[50] McKeown R, Ostilla-M´onico R, Pumir A, Brenner MP, Rubinstein SM. Turbulence generation through an iterative cascade of the elliptical instability. Sci Adv 2020;6 (9):eaaz 2717.

[51] Dong X, Tian S, Liu C. Correlation analysis on volume vorticity and vortex in late boundary layer transition. Phys Fluids 2018;30(1):014105.

[52] Perry, A.E. and Chong, M.S. (1982). "A description of eddying motions and flow patterns using critical-point concepts." Annual Review of Fluid Mechanics, 14(1), pp. 371-404.

[53] Zaki, T.A., and Durbin, P.A. (2005). A new method for the simulation of boundary-layer transition. Journal of Fluid Mechanics, 525, 1-32. [29] Corrsin, S., & Lumley, J. L. (2010). The Structure of Turbulent Shear Flow. Cambridge University Press.

[54] Perry, A.E. and Chong, M.S. (1982). "A description of eddying motions and flow patterns using critical-point concepts." Annual Review of Fluid Mechanics, 14(1), pp. 371-404.

[55] Zaki, T.A., and Durbin, P.A. (2005). A new method for the simulation of boundary-layer transition. Journal of Fluid Mechanics, 525, 1-32.

[56] Corrsin, S., & Lumley, J. L. (2010). The Structure of Turbulent Shear Flow. Cambridge University Press.

[57] Nikuradse, J. and von Kármán, T. (1933). The Law of the Wall in Turbulent Shear Flow. Technical Report, National Advisory Committee for Aeronautics, Washington D.C.

[58] Abe, Hiroyuki et al. “Direct Numerical Simulation of a Fully Developed Turbulent Channel Flow With Respect to the Reynolds Number Dependence.” *Journal of Fluids Engineering-transactions of The Asme* 123 (2001): 382-393.

BIOGRAPGHICAL INFORMATION

Vishwa was born in Gujarat, India and she has settled down in USA. She received her B.Sc. in Mathematics from The Maharaja Sayajirao University of Baroda, India in 2015 and M.Sc. in Pure Mathematics from The Maharaja Sayajirao University of Baroda, India in 2017. She has earned the Benny M. McCarley Scholarship from the Department of Mathematics in 21-22. Her research interests include numerical methods, the applications in Computational Fluid Dynamics, computational mathematics. She will be pursuing her future in academics.